Analytical Determination of Conduction and Switching Power Losses in Flying-Capacitor-Based Active Neutral-Point-Clamped Multilevel Converter

Arash Khoshkbar Sadigh, *Member, IEEE*, Vahid Dargahi, *Student Member, IEEE*, and Keith A. Corzine, *Senior Member, IEEE*

***Abstract*—Multilevel converters are mainly used in medium-voltage high-power applications. Active neutral-point-clamped (ANPC) flying capacitor multicell (FCM) converter is a well-known type of multilevel converters which is commercially available in high-power medium-voltage motor drive market. Since power loss investigation can be very advantageous in the design phase of multilevel converters, this paper presents an analytical approach to calculate and investigate the conduction and switching power loss in ANPC-FCM converter. First, the RMS and average currents of insulated-gate bipolar transistors (IGBTs) and antiparallel diodes are analytically calculated by considering the associated duty cycle of each IGBT and diode, converter modulation index, load current, and load power factor. Numerical results of the derived closed-form equations to calculate the RMS and average currents of IGBTs/diodes are compared with simulation results and experimental measurements. Numerical results match the simulation results and experimental measurements which validates the derived closed-form equations. Afterward, the obtained equations for RMS and average current computations are utilized to calculate the conduction power losses in a 12.1-MVA 6.6-kV nine-level (line-to-line) ANPC-FCM multilevel converter. For this purpose, a 4.5-kV 1.2-kA IGBT module from ABB is considered as a power switch and its parameters are employed in analytical computations and simulation of the ANPC-FCM multilevel converter for conduction power loss determination. Moreover, closed-form equations are derived for analytical determination of switching power losses for ANPC-FCM converter using Kapteyn (Fourier-Bessel) series. Based on the derived closed-form equations for conduction loss and switching loss calculation, a method is presented to determine the junction temperature in IGBTs and diodes for ANPC-FCM converter.**

***Index Terms*—Active neutral point clamped converter, closed-form equations, conduction power loss, flying capacitor multicell converter, multilevel converter, switching power loss.**

I. Introduction

Multilevel inverters/converters are the most cost-effective solutions and the state-of-the-art topologies for medium-voltage high-power applications of power electronic converters in the efficient energy conversion arena [1], [2]. These converters are particularly designed to be employed in energy and power conversion areas requiring high efficiency at higher switching frequencies, high power demand, and augmented power quality [3]. The neutral point clamped (NPC) [4], cascaded H-bridge (CHB) [5], modular multilevel converter (MMC) [6], flying capacitor multicell (FCM) [7], and active neutral point clamped (ANPC) [8] are the most common and commercialized topologies and breeds of multilevel converters powering a wide range of applications in industry [9]–[11]. The most noteworthy advantages and features of multilevel converters are notable enhanced power quality, reduced size of output filters, high modularity, fault tolerant, and extended power range [12]–[15].

Power conversion through power electronic converters/inverters employing semiconductor devices exhibiting internal inherent characteristics such as on-state resistance, forward voltage drop, and turn-on and turn-off energy losses, account for slightly dropped efficiency and some energy losses inside these power converters. Generally, converter losses can be split into switching and conduction losses. The turn-on and turn-off energy losses due to switching delays that are intrinsic to the semiconductor device account for the switching loss of the converters [16]–[23]. In order to calculate the switching losses, it is essential to estimate the operating point turn-on and turn-off energy losses of the insulated-gate bipolar transistors (IGBTs) and diodes by interpolation technique and using the turn-on and turn-off energy loss data corresponding to the phase voltage and current waveform test points provided in the device datasheet. It is noteworthy that the turn-on and turn-off energy loss data for IGBT and diode available through datasheet are generally given for a switching period. Hence, these one-switching period switching energy losses must be multiplied by the converter switching frequency for the total switching losses. So, the total switching losses are dependent on the converter switching frequency and switching characteristics of the employed semiconductors [8], [23]–[27]. The on-state resistance and voltage drop across the IGBT and diode account for the conduction losses in the power converters. The conduction power losses are calculated with obtaining the required characteristics of the on-state resistance and forward voltage drop from datasheet of the IGBT and diode through linearization method and the corresponding average and RMS current of the phase current waveform [21], [23], [24], [28].

The converter switching and conduction power loss calculation, comparative study, and efficiency evaluation of the commercially available medium-voltage drives using three-phase

Manuscript received January 29, 2015; revised July 11, 2015; accepted September 6, 2015. Date of publication November 5, 2015; date of current version March 2, 2016. Recommended for publication by Associate Editor J. R. Rodriguez.

A. Khoshkbar. Sadigh is with Extron Electronics, Anaheim, CA 92805 USA (e-mail: a.khoshkbar.sadigh@gmail.com).

V. Dargahi and K. Corzine are with the Microgrid and Power Electronics Laboratory, Holcombe Department of Electrical and Computer Engineering, Clemson University, Clemson, SC 29634 USA (e-mail: vdargah@clemson.edu; Keith@Corzine.net).

Color versions of one or more of the figures in this paper are available online at http://ieeexplore.ieee.org.

Digital Object Identifier 10.1109/TPEL.2015.2498107

two-level (e.g., Converteam) and multilevel converters such as three-level NPC (e.g., ABB, Converteam, Siemens), three-level and four-level FCM (e.g., Converteam), and nine-level CHB (e.g., Siemens) are given in [29] whereas all confirming the enhanced efficiency and improved characteristics of the multilevel power converters. The IGBT and diodes current requirements and their switching and conduction power loss estimation under new modulation technique for MMCs is investigated in [23]. It is shown that the lower IGBT module generates substantially higher losses than the upper one for all investigated load phase angles. Switching loss evaluation of a 4.5-kV–5.5-kA integrated gate-commutated thyristor within a three-level ANPC converter phase leg for a current range from 1 to 4.5 kA and junction temperatures between 25°C and 125 °C considering different commutation states and associated energies involved in the switching transients are investigated in [8] and [27] using the proposed switching loss model. Calculation of the switching and conduction power losses with measured voltage and current waveforms of the operating point and data collected from datasheet using curve-fitting and interpolation techniques (not closed-form equations) for advanced multilevel converters such as T-type, hybrid NPC, and ANPC are investigated in [19], [22], [24], [26], [30] whereas closed form equations and optimal modulation techniques for minimizing conduction power losses of the dual active bridge converters is discussed in [28]. Start-up and switching loss reduction is discussed for FCM converters in [31] where it exploits fewer switching states to reduce the switching losses.

One of the recently commercialized breeds of the FCM-based multilevel converters is ANPC-FCM which is introduced by ABB [32]–[35]. The ANPC-FCM converter is a hybrid topology based on combination of NPC and FCM converters which combines, employs, and features advantages of the both converters [22], [36]–[39]. This converter is a well-established topology in the MV drive market. For example, ANPC-FCM technology has now been matured into ACS2000 MV drive constructed by ABB [33], [34]. For appropriate design of multilevel converters, it is a concern of utmost importance and practical interest to calculate both conduction and switching losses of IGBTs/diodes in order to select IGBTs/diodes properly for specific power range without exceeding the maximum temperature rating of semiconductors. It is noteworthy that analytical calculation of both conduction and switching losses is advantageous in the design procedure. All of the available research articles in this topic have investigated the conduction and switching power losses of multilevel converters through simulation/experimental [8], [16]–[18], [20], [21], [23], [27], [40]–[42]. Using simulation/experimental results for investigation of the power losses is time consuming and arduous task since the circuit needs to be run for numerous cases considering different values of modulation index and load power factor (PF). Taking into account the advantages of ANPC-FCM converters and their escalating utilization in MV drive market and renewable energy applications necessitates investigation of the ANPC-FCM converter's performance and efficiency with any number of switching-power-cell and voltage levels as a function of the converter output power, load PF, and modulation index. Hence, this paper presents an analytical approach to calculate and investigate the conduction power losses in ANPC-FCM converters. This paper is organized as follows. Section II discusses about the conduction power loss calculation of IGBT/diode. Moreover, the approach to obtain the parameters of IGBTs/diodes from datasheet for conduction power loss calculation is discussed. Section III presents a detailed approach to analytically calculate the RMS and average currents flowing through IGBTs/diodes as a function of load peak current, load PF, and modulation index in ANPC-FCM converter. In Section IV, the numerical results of the derived analytical equations to calculate the RMS and average current of IGBTs/diodes are compared with simulation and experimental results to validate the derived analytical equations. Finally, utilizing the derived closed-form equations, Section V investigates the conduction power losses for 12.1-MVA 6.6-kV nine-level (line-to-line) ANPC-FCM converter. For the accomplished case study for ANPC-FCM converter, the parameters of a 5SNA 1200G450300 HiPak 4.5-kV 1.2-kA IGBT module are considered and also comparative illustration of conduction power losses are presented. Moreover, closed-form equations are derived in Section VI for analytical determination of switching power losses for ANPC-FCM converter using Kapteyn (Fourier-Bessel) series. Based on derived closed-form equations for conduction and switching loss calculation, a method is presented in Section VII to calculate junction temperature of semiconductors for ANPC-FCM converter analytically.

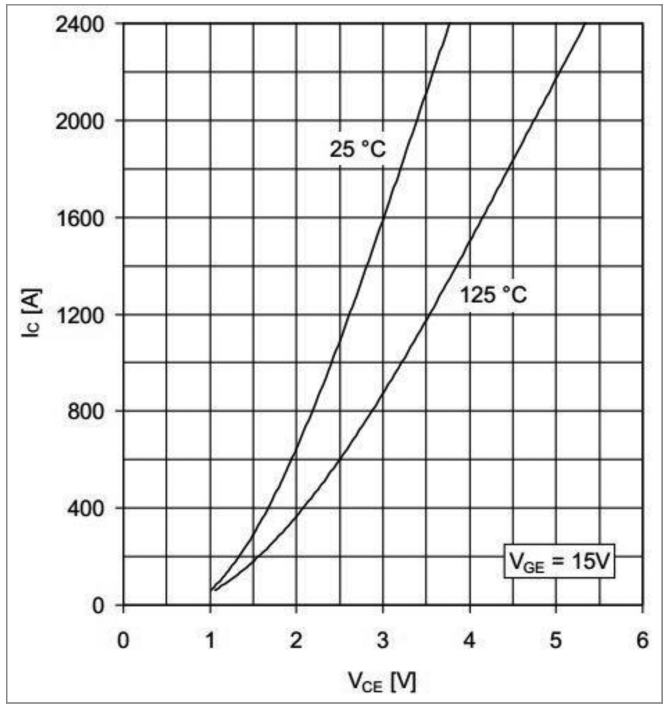

Fig. 1. Obtaining v_{CE0} and R_C from the datasheet by polynomial approximation.

II. Analytical Calculation of the Conduction Power Losses in IGBTs and Antiparallel Diodes

Analytical equations expressing the conduction power losses associated with the switching devices in the multilevel converters are very advantageous in the design procedure of these

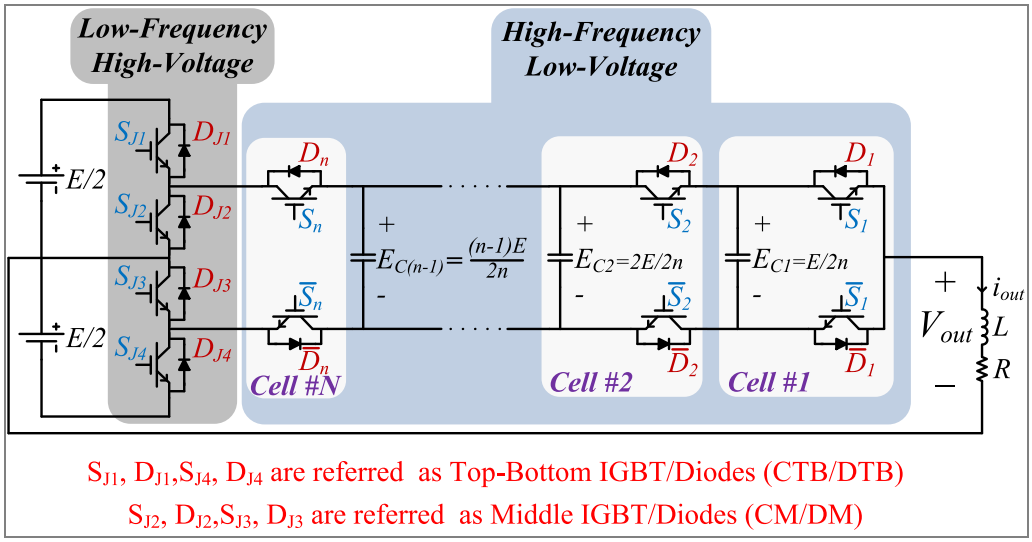

Fig. 2. General topology of a single-phase *n*-cell *2n+1*-level ANPC-FCM converter.

TABLE I
FIRST-, SECOND-, AND THIRD-ORDER APPROXIMATION OF IGBT 5SNA 1200G450300 COLLECTOR–EMITTER VOLTAGE DROP

First Order	$v_{\mathrm{CE}} = 1.28 + 17.63 \times 10^{-4} \times \mathrm{I}_C$
Second Order	$v_{\mathrm{CE}} = 1.02 + 24.79 \times 10^{-4} \times \mathrm{I}_C - 29.85 \times 10^{-8} \times \mathrm{I}_C^2$
Third Order	$v_{\mathrm{CE}} = 0.9035 + 32 \times 10^{-4} \times \mathrm{I}_C - 10.86 \times 10^{-8} \times \mathrm{I}_C^2 + 21.89 \times 10^{-11} \times \mathrm{I}_C^3$

power converters. The power loss analytical equations can be used to investigate converters' performance and efficiency with any number of switching-power-cell and voltage levels as a function of the converter output power, load PF, and modulation index. In this section, an analytical approach to calculate the conduction power loss in both IGBT and diode is discussed. The IGBT collector–emitter voltage drop (v_{CE}) when it is conducting is shown in Fig. 1 which is related to 5SNA 1200G450300. In order to use these data, two options are available. The first option is using the real data curve from datasheet. In order to do this, data are read from datasheet for each interval of 200 A and saved. For values between 200 A interval, it can be interpolated. This way, the real data curve can be utilized. Although this method results in the minimum error, it needs lookup table and more calculations. Another option is to approximate the real data curve which can be the first order, second order, and so on. Herein, conduction power loss for a single high-frequency IGBT (S1) in ANPC-FCM converter, whose general structure is shown in Fig. 2, is obtained using the real curve data from datasheet shown in Fig. 1. Afterward, conduction power loss for the same power switch (S1) is obtained using first-, second-, and third-order approximations. The coefficients of the approximations obtained through Matlab are listed in Table I. It should be mentioned that the junction temperature is considered $125^{\circ}\mathrm{C}$ in all coefficients listed with Table I.

The conduction power losses obtained from approximation of collector–emitter voltage drop compared in difference case studies with conduction power loss based on real curve data from datasheet. The comparison is listed in Table II where the first-order approximation has the maximum error of 5% regarding the real date curve from the datasheet. However, the first-order approximation in some cases has almost the same or even less amount of error in comparison with second or third approximation. This shows that first-order (linear) approximation is an acceptable approximation.

TABLE II
CONDUCTION POWER LOSS COMPARISON BETWEEN FIRST-, SECOND-, AND THIRD-ORDER APPROXIMATION OF COLLECTOR–EMITTER VOLTAGE DROP AND REAL CURVE DATA FROM DATASHEET OF IGBT 5SNA 1200G450300

Case Study Condition	Real Curve Data (W)	Error of First-Order Approximation (%)	Error of Second-Order Approximation (%)	Error of Third-Order Approximation (%)
Ipeak = 1500 A, PF = 0.87, M = 0.9	1139.72	3.44	0.62	0.14
Ipeak = 1500 A, PF = 0.87, M = 0.7	904.76	3.81	0.55	0.12
Ipeak = 1500 A, PF = 0.87, M = 0.5	664.66	3.30	0.31	0.06
Ipeak = 1500 A, PF = 0.7, M = 0.8	963.16	3.46	0.40	0.24
Ipeak = 1200 A, PF = 0.7, M = 0.8	685.31	4.68	0.72	0.41
Ipeak = 500 A, PF = 0.7, M = 0.8	188.54	2.35	4.32	1.87
Ipeak = 1000 A, PF = 0.7, M = 0.8	519.59	4.91	1.54	0.49
Ipeak = 1000 A, PF = 0.5, M = 0.5	383.26	4.96	1.85	0.38
Ipeak = 800 A, PF = 0.5, M = 0.5	275.83	4.92	3.15	0.39
Ipeak = 500 A, PF = 0.5, M = 0.5	139.51	2.10	4.33	2.02

Since the first-order approximation is close enough to the real curve data, the IGBT collector–emitter voltage drop (v_{CE}) when it is conducting at a specific junction temperature can be written as follows:

$$v_{\mathrm{CE}} = v_{\mathrm{CE0}} + R_C \cdot i_C \tag{1}$$

where v_{CE0} is representing the IGBT on-state zero-current collector–emitter forward voltage drop and R_C is collector–emitter on-state resistance. The same approximation at a specific junction temperature can be used for the antiparallel diode, giving

$$v_F = v_{F0} + R_F \cdot i_F \tag{2}$$

where v_{F0} is representing the antiparallel diode on-state zero-current forward voltage drop and R_F is antiparallel diode on-state resistance. These important parameters can be obtained directly from the IGBT datasheet.

The instantaneous values of the IGBT conduction losses $(p_{\mathrm{CT}}(t))$ and the average losses (P_{CT}) are

$$p_{\mathrm{CT}}(t) = v_{\mathrm{CE}}(t) \cdot i_C(t) = v_{\mathrm{CE0}} \cdot i_C(t) + R_C \cdot i_C^2(t) \tag{3}$$

$$P_{\mathrm{CT}} = \frac{1}{2\pi}\int_0^{2\pi} [p_{\mathrm{CT}}(t)]\, d(\omega t)$$

$$= \frac{1}{2\pi}\int_0^{2\pi} \left[v_{\mathrm{CE0}} \cdot i_C(t) + R_C \cdot i_C^2(t)\right] d(\omega t) \tag{4}$$

$$P_{\mathrm{CT}} = v_{\mathrm{CE0}} \cdot I_{C,\mathrm{avg}} + R_C \cdot I_{C,\mathrm{rms}}^2 \tag{5}$$

where $I_{C,\mathrm{avg}}$ and $I_{C,\mathrm{rms}}$ are the average and RMS currents of the IGBT, respectively. Similar to the IGBT, the average value of the diode conduction losses (P_{CD}) is

$$P_{\mathrm{CD}} = v_{F0} \cdot I_{D,\mathrm{avg}} + R_F \cdot I_{D,\mathrm{rms}}^2 \tag{6}$$

where $I_{D,\mathrm{avg}}$ and $I_{D,\mathrm{rms}}$ are the average and RMS currents of antiparallel diode, respectively.

In (1) and (2), voltage drops of both IGBT and diode which are based on first-order approximation of real curve data are for a specific junction temperature. However, these values are also dependent of junction temperature which is different for each case and semiconductor where amount of conduction and switching losses determine the junction temperature of each individual semiconductor device. For example, high-frequency semiconductors in comparison with low-frequency semiconductors have much higher switching losses. Thus, the junction temperature of the high-frequency semiconductors is higher than the low-frequency semiconductors. Consequently, the effect of junction temperature on voltage drops of both IGBT and diode should be considered resulting in following equations:

$$v_{\mathrm{CE}@T} = \underbrace{(v_{\mathrm{CE0\_}K0} + v_{\mathrm{CE0\_}K1} \cdot T)}_{v_{\mathrm{CE0}@T}} + \underbrace{(R_{C\_K0} + R_{C\_K1} \cdot T)}_{R_{C@T}} \cdot i_C \tag{7}$$

$$v_{F@T} = \underbrace{(v_{F0\_K0} + v_{F0\_K1} \cdot T)}_{v_{F0@T}} + \underbrace{(R_{F\_K0} + R_{F\_K1} \cdot T)}_{R_{F@T}} \cdot i_C \tag{8}$$

where, $v_{\mathrm{CE}@T}$ and $v_{F@T}$ are first-order approximation of voltage drop IGBT and diode, respectively, at junction temperature of T^oC. From datasheet of 5SNA 1200G450300, thermal coefficient of $v_{\mathrm{CE0}@T}$ and $R_{C@T}$ for IGBT and $v_{F0@T}$ and $R_{F@T}$ are obtained and listed in Table III for two temperatures of 25° and 125°C according to the datasheet. Afterward, the rest of thermal coefficients are obtained using the following equations

TABLE III
THERMAL COEFFICIENTS OF FIRST-ORDER APPROXIMATION OF VOLTAGE DROP OF IGBT AND DIODE 5SNA 1200G450300

IGBT		Diode	
$v_{\mathrm{CE}@25}$	1.16 V	$v_{F0@25}$	1.94 V
$R_{C@25}$	1.14 mΩ	$R_{F@25}$	0.9 mΩ
$v_{\mathrm{CE}@125}$	1.28 V	$v_{F0@125}$	1.76 V
$R_{C@125}$	1.76 mΩ	$R_{F@125}$	1.26 mΩ
$v_{\mathrm{CE0\_}K0}$	1.13 V	v_{F0_K0}	1.99 V
$v_{\mathrm{CE0\_}K1}$	1.2 mV/°C	v_{F0_K1}	–1.9 mV/°C
R_{C_K0}	0.98 mΩ	R_{F_K0}	0.8 mΩ
R_{C_Kl}	6.25 uΩ/°C	R_{F_K1}	3.61 uΩ/°C

and are listed in Table III:

$$v_{\mathrm{CE0\_}K0} = \frac{v_{\mathrm{CE0}@T_2} \cdot T_1 - v_{\mathrm{CE0}@T_1} \cdot T_2}{T_1 - T_2} \tag{9}$$

$$v_{\mathrm{CE0\_}K1} = \frac{v_{\mathrm{CE0}@T_1} - v_{\mathrm{CE0}@T_2}}{T_1 - T_2} \tag{10}$$

$$R_{C\_K0} = \frac{R_{C@T_2} \cdot T_1 - R_{C@T_1} \cdot T_2}{T_1 - T_2} \tag{11}$$

$$R_{C\_K1} = \frac{R_{C@T_1} - R_{C@T_2}}{T_1 - T_2} \tag{12}$$

$$v_{F0\_K0} = \frac{v_{F0@T_2} \cdot T_1 - v_{F0@T_1} \cdot T_2}{T_1 - T_2} \tag{13}$$

$$v_{F0\_K1} = \frac{v_{F0@T_1} - v_{F0@T_2}}{T_1 - T_2} \tag{14}$$

$$R_{F\_K0} = \frac{R_{F@T_2} \cdot T_1 - R_{F@T_1} \cdot T_2}{T_1 - T_2} \tag{15}$$

$$R_{F\_K1} = \frac{R_{F@T_1} - R_{F@T_2}}{T_1 - T_2} \tag{16}$$

where, T_1 and T_2 are 25° and 125°C, respectively, according to the datasheet. Finally, dependency of IGBT and diode conduction power loss on the junction temperature can be modeled as follows:

$$P_{\mathrm{CT}}(I_C, T) = (v_{\mathrm{CE0\_}K0} + v_{\mathrm{CE0\_}K1} \cdot T) \cdot I_{C,\mathrm{avg}} + (R_{C\_K0} + R_{C\_K1} \cdot T) \cdot I_{\mathrm{C,rms}}^2 \tag{17}$$

$$P_{\mathrm{CD}}(I_F, T) = (v_{F0\_K0} + v_{F0\_K1} \cdot T) \cdot I_{D,\mathrm{avg}} + (R_{F\_K0} + R_{F\_K1} \cdot T) \cdot I_{D,\mathrm{rms}}^2. \tag{18}$$

As it can be seen in (17) and (18), it is required to obtain the average and RMS current flowing through IGBT and diode in order to calculate their conduction power losses. First contribution of this paper is deriving the analytical equations expressing average and RMS currents of semiconductors, i.e., IGBT and diode, in terms of load PF, load peak current, and modulation index which are explained in the following sections. As it will be demonstrated later, in order to have a good estimation of conduction losses, the junction temperature for each IGBT and diode must be calculated. To evaluate the junction temperature of the semiconductor devices and also to investigate the total efficiency of the power converters, switching power loss must be considered and computed. Hence, this paper derives closed-form

equations in order to analytically calculate the switching power losses exploiting the Kapteyn (Fourier-Bessel) series.

III. Average and RMS Current Calculation of IGBTs and Antiparallel Diodes in ANPC-FCM Converter

In this section, an analytical approach is presented to calculate the average and RMS current flowing through the IGBTs/diodes in ANPC-FCM converter. Afterward, obtained analytical equations to calculate the average and RMS current of IGBTs/diodes are utilized to investigate the conduction power loss in ANPC-FCM converter whose general topology is shown in Fig. 2.

For the sake of simplicity in deriving analytical equations for average and RMS currents, the phase current can be assumed to be sinusoidal. The actual current waveform is slightly distorted by pulse-width modulation (PWM) high-frequency ripple current and motor nonlinearity in motor drive application. The phase current for an induction motor, as an example, normally lags the phase voltage by the phase angle φ. Because the current is a simple sine function, the math works out to be much easier if the voltage is assumed to lead the current by φ, and integrate over the current waveform. The resulting relationships are the same using either method. Power semiconductors in the ANPC-FCM converter can be categorized as follows [8], [27], [32]–[34], [43]:

1) low-frequency IGBTs/diodes (S_{J1} to S_{J4}, and D_{J1} to D_{J4});
2) high-frequency IGBTs/diodes (S_1 to S_n, and D_1 to D_n).

It is worth mentioning that low-frequency IGBTs/diode are ON for first half- cycle of line frequency and OFF for the other half-cycle of line frequency whereas the high-frequency IGBTs/diodes turn on and turn off during full-cycle of line frequency. Fig. 3 illustrates the duty cycle $(D_{\mathrm{LF}}(t))$of low-frequency IGBTs/diodes, duty cycle $(D_{\mathrm{HF}}(t))$of high-frequency IGBTs/diodes, and the relationship between the phase voltage, phase current, and the duty cycle. Thus, the phase current $(i_\phi(t))$and duty cycle of switches are defined according to the following equations:

$$i_\phi(t) = I_P \cdot \sin(\omega t) \tag{19}$$

$$D_{\mathrm{HF}}(t) = \begin{cases} M\sin(\omega t+\varphi) & -\varphi < \omega t < \pi-\varphi \\ 1+M\sin(\omega t+\varphi) & \pi-\varphi < \omega t < 2\pi-\varphi \end{cases} \tag{20}$$

$$D_{\mathrm{LF}}(t) = \begin{cases} 1 & -\varphi < \omega t < \pi-\varphi \\ 0 & \pi-\varphi < \omega t < 2\pi-\varphi \end{cases} \tag{21}$$

where I_{P} is the peak current, M is the modulation index, $\omega = 2\pi f$ is the angular frequency, and f is the output voltage frequency. The modulation index represents the normalized voltage and it is between zero and one. When low-frequency IGBTs/diodes are ON, they are in series with high-frequency IGBTs/diodes. Therefore, the effective duty cycle of low-frequency IGBTs/diodes $(D_{\mathrm{TB}}(t), D_M(t))$ should be obtained by multiplication of actual duty cycle of low-frequency IGBTs/diodes with the duty cycle of related high-frequency IGBTs/diodes. However, the duty cycle of high-frequency IGBTs/diodes S_n, D_n in cell #*n* do not need to be modified since the duty cycle of low-frequency IGBTs/diodes (whenever is ON) is 1. Thus, it will not impact the effective duty cycle of

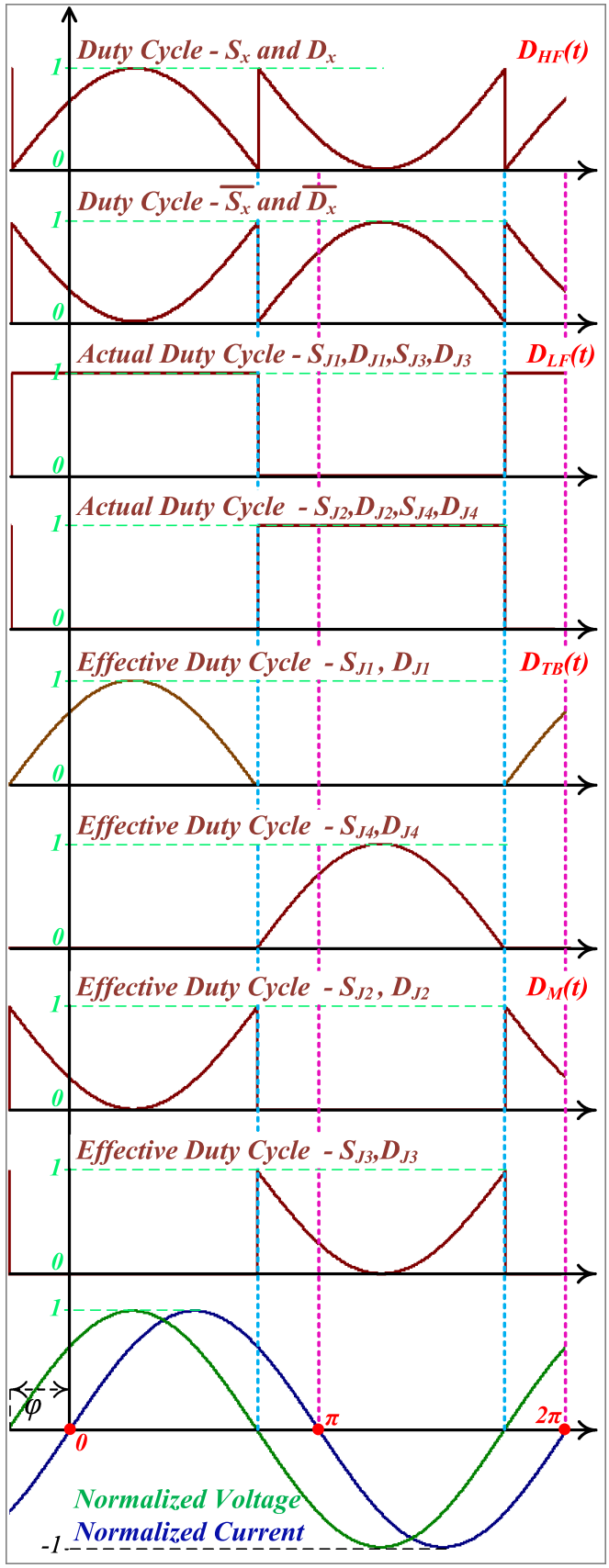

Fig. 3. Normalized value of phase voltage, phase current, and duty cycle of IGBTs and diodes in the ANPC-FCM converter.

high-frequency IGBTs/diodes S_n, D_n in cell #n. Following are the effective duty cycle of low-frequency IGBTs/diodes:

$$D_{\mathrm{TB}}(t) = \begin{cases} M\sin(\omega t+\varphi) & -\varphi < \omega t < \pi-\varphi \\ 0 & \pi-\varphi < \omega t < 2\pi-\varphi \end{cases} \quad (22)$$

$$D_M(t) = \begin{cases} 1-M\sin(\omega t+\varphi) & -\varphi < \omega t < \pi-\varphi \\ 0 & \pi-\varphi < \omega t < 2\pi-\varphi \end{cases}. \quad (23)$$

It is worth mentioning that due to the symmetrical operation of top and bottom high-frequency IGBTs/diodes (S_x, D_x and $\overline{S_x}, \overline{D_x}$) in each cell, they have the same average and RMS current rating. Therefore, the calculations are done only for top high-frequency IGBTs/diodes (S_x, D_x) and extended to the bottom IGBTs/diodes ($\overline{S_x}, \overline{D_x}$). Likewise, the calculations are done for top low-frequency IGBT/Diode (S_{J1}, D_{J1}) and middle low-frequency IGBT/Diode (S_{J2}, D_{J2}) and extended to the bottom low-frequency IGBT/Diode (S_{J4}, D_{J4}) and another middle low-frequency IGBT/Diode (S_{J3}, D_{J3}), respectively.

The top high-frequency IGBT carries the current whenever it is ON ($D_{\mathrm{HF}}(t)$)as well as the phase current is positive which is for ωt from 0 to π. Moreover, the top high-frequency antiparallel diode carries the current whenever its associated IGBT gate signal is ON ($D_{\mathrm{HF}}(t)$)as well as the phase current is negative which is for ωt from π to 2π. The average IGBT and diode currents over the full sin wave can then be found by integrating the duty cycle times, the phase current, and opposite of phase current, respectively. Therefore, by assuming that the phase current is almost constant over one PWM cycle, the average current of top high-frequency IGBT can be calculated as follows:

$$\begin{aligned} I_{\mathrm{CHF,avg}} &= \frac{1}{2\pi}\int_0^{\pi}[i_\phi(t)\cdot D_{\mathrm{HF}}(t)]\,d(\omega t) \\ &= \frac{1}{2\pi}\int_0^{\pi-\varphi}[(I_P\sin(\omega t))\cdot(M\sin(\omega t+\varphi))]\,d(\omega t) \\ &+\frac{1}{2\pi}\int_{\pi-\varphi}^{\pi}[(I_P\sin(\omega t))\cdot(1+M\sin(\omega t+\varphi))]\,d(\omega t). \end{aligned} \quad (24)$$

Equation (24) can be simplified furthermore as (25)

$$\begin{aligned} I_{\mathrm{CHF,avg}} &= \frac{I_P M}{4\pi}(\pi-\varphi)\cos(\varphi)+\frac{I_P M}{4\pi}\sin(\varphi) \\ &+\frac{I_P}{2\pi}(1-\cos(\varphi))+\frac{I_P M\varphi}{4\pi}\cos(\varphi)-\frac{I_P M}{4\pi}\sin(\varphi) \\ &= \frac{I_P M}{4}\cos(\varphi)+\frac{I_P}{2\pi}(1-\cos(\varphi)). \end{aligned} \quad (25)$$

By following the same procedure, the top high-frequency diode average current can be obtained as follows:

$$\begin{aligned} I_{\mathrm{DHF,avg}} &= \frac{1}{2\pi}\int_{\pi}^{2\pi}[(-i_\phi(t))\cdot D_{\mathrm{HF}}(t)]\,d(\omega t) \\ &= \frac{1}{2\pi}\int_{\pi}^{2\pi-\varphi}[(-I_P\sin(\omega t))\cdot(1+M\sin(\omega t+\varphi))]\,d(\omega t) \\ &+\frac{1}{2\pi}\int_{2\pi-\varphi}^{2\pi}[(-I_P\sin(\omega t))\cdot(M\sin(\omega t+\varphi))]\,d(\omega t). \end{aligned} \quad (26)$$

Equation (26) can be rewritten as (27)

$$\begin{aligned} I_{\mathrm{DHF,avg}} &= \frac{I_P}{2\pi}(1+\cos(\varphi))-\frac{I_P M}{4\pi}(\pi-\varphi)\cos(\varphi) \\ &-\frac{I_P M}{4\pi}\sin(\varphi)-\frac{I_P M\varphi}{4\pi}\cos(\varphi)+\frac{I_P M}{4\pi}\sin(\varphi) \\ &= \frac{I_P}{2\pi}(1+\cos(\varphi))-\frac{I_P M}{4}\cos(\varphi). \end{aligned} \quad (27)$$

Similarly, the average current of top/bottom low-frequency IGBT and diode can be obtained as follows:

$$\begin{aligned} I_{\mathrm{CTB,avg}} &= \frac{1}{2\pi}\int_0^{\pi}[i_\phi(t)\cdot D_{\mathrm{TB}}(t)]\,d(\omega t) \\ &= \frac{1}{2\pi}\int_0^{\pi-\varphi}[(I_P\sin(\omega t))\cdot(M\sin(\omega t+\varphi))]\,d(\omega t) \\ &= \frac{I_P M}{4\pi}((\pi-\varphi)\cos(\varphi)+\sin(\varphi)) \end{aligned} \quad (28)$$

$$\begin{aligned} I_{\mathrm{DTB,avg}} &= \frac{1}{2\pi}\int_{\pi}^{2\pi}[(-i_\phi(t))\cdot D_{TB}(t)]\,d(\omega t) \\ &= \frac{1}{2\pi}\int_{2\pi-\varphi}^{2\pi}[(-I_P\sin(\omega t))\cdot(M\sin(\omega t+\varphi))]\,d(\omega t) \\ &= \frac{I_P M}{4\pi}(\sin(\varphi)-\varphi\cos(\varphi)). \end{aligned} \quad (29)$$

The same way, the average current of middle low-frequency IGBT and diode can be obtained as follows:

$$\begin{aligned} I_{\mathrm{CM,avg}} &= \frac{1}{2\pi}\int_0^{\pi}[i_\phi(t)\cdot D_M(t)]\,d(\omega t) \\ &= \frac{1}{2\pi}\int_0^{\pi-\varphi}[(I_P\sin(\omega t))\cdot(1-M\sin(\omega t+\varphi))]\,d(\omega t) \\ &= \frac{I_P}{2\pi}(1+\cos(\varphi))-\frac{I_P M}{4\pi}(\sin(\varphi)+(\pi-\varphi)\cos(\varphi)) \end{aligned} \quad (30)$$

$$\begin{aligned} I_{\mathrm{DM,avg}} &= \frac{1}{2\pi}\int_{\pi}^{2\pi}[(-i_\phi(t))\cdot D_M(t)]\,d(\omega t) \\ &= \frac{1}{2\pi}\int_{2\pi-\varphi}^{2\pi}[(-I_P\sin(\omega t))\cdot(1-M\sin(\omega t+\varphi))]\,d(\omega t) \\ &= \frac{I_P}{2\pi}(-1+\cos(\varphi))-\frac{I_P M}{4\pi}(\sin(\varphi)-\varphi\cos(\varphi)). \end{aligned} \quad (31)$$

As the final step, the RMS current of the top high-frequency IGBT can be calculated as (32) as shown at the bottom of next page.

Before continuing to calculate the integral of (32), it is worth mentioning the reason that term $D_{\mathrm{HF}}(t)$ is not squared in (32) while only $i_\varphi(t)$ is squared. The RMS value of high-frequency IGBT current shown in Fig. 4, is calculated as follows:

$$\begin{aligned} I_{\mathrm{rms}} &= \sqrt{\frac{1}{T_{\mathrm{line}}}\int_0^{T_{\mathrm{line}}}[i^2_{\mathrm{CHF}}(t)]\,d(t)} \\ &= \sqrt{\frac{1}{T_{\mathrm{line}}}(I_1^2D_1T_S+I_2^2D_2T_S+\cdots+I_n^2D_nT_S)} \\ &= \sqrt{\frac{1}{n}(I_1^2D_1+I_2^2D_2+\cdots+I_n^2D_n)} \end{aligned} \quad (33)$$

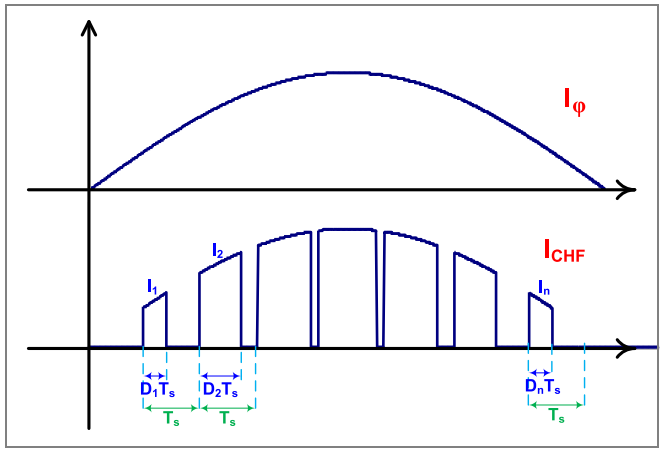

Fig. 4. Illustration of RMS current calculation for high-frequency IGBT.

where, $I_K = i_\phi[K]$ which means that I_K equals to time-domain load current ($i_\phi(t)$) at K^{th} switching cycle. Similarly, $D_K = D_{\text{HF}}[K]$ which means that D_K equals to time-domain duty cycle ($D_{\text{HF}}(t)$) at K^{th} switching cycle. Therefore, (33) can be written as follows:

$$I_{\text{rms}} = \sqrt{\frac{1}{n}\sum_{k=1}^{n} i_\phi^2[n]\, D_{\text{HF}}[n]}. \tag{34}$$

Equation (34) which is in discrete domain can be converted to time domain as follows:

$$I_{\text{rms}} = \sqrt{\frac{1}{T_{\text{Line}}}\int_0^{T_{\text{Line}}} \left[i_\phi^2(t)\, D_{\text{HF}}(t)\right] d(t)} = \sqrt{\frac{1}{2\pi}\int_0^{\pi} \left[i_\phi^2(t)\cdot D_{\text{HF}}(t)\right] d(\omega t)}. \tag{35}$$

This is the reason why term $D_{\text{HF}}(t)$ is not squared in (32) whereas only $i_\phi(t)$ is squared.

Hence, (32) is simplified furthermore as (36), shown at the bottom of the page

By following the same procedure, the RMS current of the top high-frequency diode can be obtained as follows:

$$I_{\text{DHF,rms}} = \sqrt{\frac{1}{2\pi}\int_{\pi}^{2\pi} \left[(-i_\phi(t))^2 \cdot D_{\text{HF}}(t)\right] d(\omega t)} = \sqrt{\begin{array}{l}\frac{1}{2\pi}\int_{\pi}^{2\pi-\varphi}\left[(-I_P\sin(\omega t))^2\cdot(1+M\sin(\omega t+\varphi))\right] d(\omega t) \\ +\frac{1}{2\pi}\int_{2\pi-\varphi}^{2\pi}\left[(-I_P\sin(\omega t))^2\cdot(M\sin(\omega t+\varphi))\right] d(\omega t)\end{array}}. \tag{37}$$

In the same manner, (37) is simplified furthermore as (38) and (39), shown at the bottom of the next page

$$I_{\text{DHF,rms}} = \sqrt{\begin{array}{l}\frac{1}{2\pi}\int_{\pi}^{2\pi-\varphi}\left[\frac{I_P^2}{2}(1-\cos(2\omega t))\right] d(\omega t) \\ +\frac{1}{2\pi}\int_{\pi}^{2\pi-\varphi}\left[\frac{MI_P^2}{2}(1-\cos(2\omega t))\cdot(\sin(\omega t+\varphi))\right] d(\omega t) \\ +\frac{1}{2\pi}\int_{2\pi-\varphi}^{2\pi}\left[\frac{MI_P^2}{2}(1-\cos(2\omega t))\cdot(\sin(\omega t+\varphi))\right] d(\omega t)\end{array}}. \tag{38}$$

Similarly, RMS current of top/bottom low-frequency IGBT and diode can be obtained as follows:

$$I_{\text{CTB,rms}} = \sqrt{\frac{1}{2\pi}\int_0^{\pi}\left[i_\phi^2(t)\cdot D_{\text{TB}}(t)\right] d(\omega t)} = \sqrt{\frac{1}{2\pi}\int_0^{\pi-\varphi}\left[(I_P\sin(\omega t))^2\cdot(M\sin(\omega t+\varphi))\right] d(\omega t)} = \sqrt{\frac{1}{2\pi}\int_0^{\pi-\varphi}\left[\frac{MI_P^2}{2}(1-\cos(2\omega t))\cdot(\sin(\omega t+\varphi))\right] d(\omega t)} = \sqrt{\frac{MI_P^2}{12\pi}\left[\cos(2\varphi)+4\cos(\varphi)+3\right]} \tag{40}$$

$$I_{\text{CHF,rms}} = \sqrt{\frac{1}{2\pi}\int_0^{\pi}\left[i_\phi^2(t)\cdot D_{\text{HF}}(t)\right] d(\omega t)} = \sqrt{\frac{1}{2\pi}\int_0^{\pi-\varphi}\left[(I_P\sin(\omega t))^2\cdot(M\sin(\omega t+\varphi))\right] d(\omega t)+\frac{1}{2\pi}\int_{\pi-\varphi}^{\pi}\left[(I_P\sin(\omega t))^2\cdot(1+M\sin(\omega t+\varphi))\right] d(\omega t)} \tag{32}$$

$$I_{\text{CHF,rms}} = \sqrt{\frac{MI_P^2}{12\pi}\left[\cos(2\varphi)+4\cos(\varphi)+3\right]+\frac{I_P^2}{8\pi}\left[2\varphi-\sin(2\varphi)\right]+\frac{MI_P^2}{12\pi}\left[-3-\cos(2\varphi)+4\cos(\varphi)\right]} = \sqrt{\frac{2MI_P^2}{3\pi}\cos(\varphi)+\frac{I_P^2}{8\pi}\left[2\varphi-\sin(2\varphi)\right]} \tag{36}$$

$$I_{\mathrm{DTB,rms}} = \sqrt{\frac{1}{2\pi}\int_{\pi}^{2\pi}\left[\left(-i_{\phi}\left(t\right)\right)^{2}\cdot D_{\mathrm{TB}}\left(t\right)\right]d\left(\omega t\right)}$$
$$= \sqrt{\frac{1}{2\pi}\int_{2\pi-\varphi}^{2\pi}\left[\left(-I_P\sin\left(\omega t\right)\right)^{2}\cdot\left(M\sin\left(\omega t+\varphi\right)\right)\right]d\left(\omega t\right)}$$
$$= \sqrt{\frac{1}{2\pi}\int_{2\pi-\varphi}^{2\pi}\left[\frac{MI_P^2}{2}\left(1-\cos\left(2\omega t\right)\right)\cdot\left(\sin\left(\omega t+\varphi\right)\right)\right]d\left(\omega t\right)}$$
$$= \sqrt{\frac{MI_P^2}{12\pi}\left[\cos\left(2\varphi\right)-4\cos\left(\varphi\right)+3\right]}. \tag{41}$$

Likewise, the RMS current of middle low-frequency IGBT and diode can be obtained as follows:

$$I_{\mathrm{CM,rms}} = \sqrt{\frac{1}{2\pi}\int_{0}^{\pi}\left[\left(i_{\phi}\left(t\right)\right)^{2}\cdot D_{M}\left(t\right)\right]d\left(\omega t\right)}$$
$$= \sqrt{\frac{1}{2\pi}\int_{0}^{\pi-\varphi}\left[\left(I_P\sin\left(\omega t\right)\right)^{2}\cdot\left(1-M\sin\left(\omega t+\varphi\right)\right)\right]d\left(\omega t\right)}$$
$$= \sqrt{\begin{array}{l}\dfrac{1}{2\pi}\displaystyle\int_{0}^{\pi-\varphi}\left[\frac{I_P^2}{2}\left(1-\cos\left(2\omega t\right)\right)\right]d\left(\omega t\right)\\ -\dfrac{1}{2\pi}\displaystyle\int_{0}^{\pi-\varphi}\left[\frac{MI_P^2}{2}\left(1-\cos\left(2\omega t\right)\right)\cdot\left(\sin\left(\omega t+\varphi\right)\right)\right]d\left(\omega t\right)\end{array}}$$
$$= \sqrt{\frac{I_P^2}{4}-\frac{I_P^2}{8\pi}\left[2\varphi-\sin\left(2\varphi\right)\right]-\frac{MI_P^2}{12\pi}\left[\cos\left(2\varphi\right)+4\cos\left(\varphi\right)+3\right]} \tag{42}$$

$$I_{\mathrm{DM,rms}} = \sqrt{\frac{1}{2\pi}\int_{\pi}^{2\pi}\left[\left(-i_{\phi}\left(t\right)\right)^{2}\cdot D_{M}\left(t\right)\right]d\left(\omega t\right)}$$
$$= \sqrt{\frac{1}{2\pi}\int_{2\pi-\varphi}^{2\pi}\left[\left(-I_P\sin\left(\omega t\right)\right)^{2}\cdot\left(1-M\sin\left(\omega t+\varphi\right)\right)\right]d\left(\omega t\right)}$$
$$= \sqrt{\begin{array}{l}\dfrac{1}{2\pi}\displaystyle\int_{2\pi-\varphi}^{2\pi}\left[\frac{I_P^2}{2}\left(1-\cos\left(2\omega t\right)\right)\right]d\left(\omega t\right)\\ -\dfrac{1}{2\pi}\displaystyle\int_{2\pi-\varphi}^{2\pi}\left[\frac{MI_P^2}{2}\left(1-\cos\left(2\omega t\right)\right)\cdot\left(\sin\left(\omega t+\varphi\right)\right)\right]d\left(\omega t\right)\end{array}}$$
$$= \sqrt{\frac{I_P^2}{8\pi}\left[2\varphi-\sin\left(2\varphi\right)\right]-\frac{MI_P^2}{12\pi}\left[\cos\left(2\varphi\right)-4\cos\left(\varphi\right)+3\right]}. \tag{43}$$

Finally, the obtained analytical expression for the average and RMS current flowing through IGBTs and diodes can be substituted in (5) and (6) to calculate the conduction power loss in ANPC-FCM converters. It is worth mentioning that one of the promising and interesting industrial applications of the ANPC-FCM voltage source converter drives is active front-end (AFE) rectifier with regenerative capability [44], [45]. As elaborated in [44], the conduction loss calculation of the NPC converter breed (also including ANPC-FCM topology) in AFE operation requires computation of average and RMS currents. Hence, the method presented in this paper can be extended to calculate average and RMS currents of the IGBTs and diodes for drive application of ANPC-FCM converters with regenerative capability. It requires modification of integral bounds in the elaborated equations.

IV. Validation of the Derived Closed-Form Equations for the Calculation of the IGBTs and Diodes Average and RMS Currents

In order to verify the derived equations for calculation of the average and RMS current flowing through IGBTs and diodes in the ANPC-FCM converter, numerical computation results of the derived equations are compared against the simulation and experimental results in two following sections.

A. Validation Through Simulation Results

The numerical computation and simulation studies are done for 12.1-MVA 6.6-kV three-phase nine-level (line-to-line) ANPC-FCM converter (comprising two high-frequency switching-power-cells per phase). In this study, a dc link of 10.8 kV which is common in all three phases is used for ANPC-FCM converter. The flying capacitor voltage in the considered case study for ANPC-FCM converter is assumed to be stabilized at 2.7 kV under proper operation. Therefore, high-frequency IGBTs in ANPC-FCM converter should withstand 2.7 kV while the low-frequency IGBTs should withstand 5.4 kV. Since the utilization factor regarding the voltage of the high-power medium-voltage switches is practically around 50% to 60%, the 4.5-kV switches are required to withstand 2.7 kV. For this purpose, ABB 5SNA 1200G450300 HiPak 4.5-kV 1.2-kA IGBT module is considered for high-frequency IGBTs. Since the voltage rating of the low-frequency IGBTs is 5.4 kV, two of the aforementioned IGBT modules which are connected in series are utilized for the low-frequency IGBTs [46]–[50]. The maximum of line peak current (I_P) is 1.5 kA in all studies to avoid the overcurrent situation in all IGBTs and diodes in the considered case for the ANPC-FCM converter.

In order to verify the derived analytical equations for the average and RMS current of IGBTs/diodes in ANPC-FCM converter, the numerical computation results are compared with the simulation results. This comparison is shown in Figs. 5–7 whereas the associated error is listed in Table IV. Figs. 5–7 and Table IV illustrate a good match between the numerical and simulation results which validates the derived analytical equations. It is worth mentioning that in this case study, load peak

$$I_{\mathrm{DHF,rms}} = \sqrt{\frac{I_P^2}{4}-\frac{I_P^2}{8\pi}\left[2\varphi-\sin\left(2\varphi\right)\right]-\frac{MI_P^2}{12\pi}\left[\cos\left(2\varphi\right)+4\cos\left(\varphi\right)+3\right]-\frac{MI_P^2}{12\pi}\left[-\cos\left(2\varphi\right)+4\cos\left(\varphi\right)-3\right]}$$
$$= \sqrt{\frac{I_P^2}{4}-\frac{I_P^2}{8\pi}\left[2\varphi-\sin\left(2\varphi\right)\right]-\frac{2MI_P^2}{3\pi}\cos\left(\varphi\right)} \tag{39}$$

TABLE IV
ERROR (%) BETWEEN THE NUMERICAL COMPUTATION AND SIMULATION RESULTS OF THE AVERAGE AND RMS CURRENTS OF IGBTS AND DIODES IN A 12.1-MVA 6.6-KV NINE-LEVEL (LINE-TO-LINE) ANPC-FCM CONVERTER

Modulation Index	I_CHF,avg Power Factor (PF)			I_DHF, avg Power Factor (PF)			I_CHF, RMS Power Factor (PF)			I_DHF,rms Power Factor (PF)		
	0.5	0.707	0.9	0.5	0.707	0.9	0.5	0.707	0.9	0.5	0.707	0.9
0.4	0.51	0.82	0.65	0.84	1.05	0.98	0.58	0.87	0.75	0.74	0.85	1.02
0.6	0.71	0.58	0.66	1.1	0.79	0.83	0.68	1.03	0.88	0.65	0.79	0.94
0.8	0.66	0.74	1.01	0.95	0.58	0.87	0.76	1.10	0.59	0.98	0.63	0.82
0.95	1.03	0.63	0.85	0.96	1.04	0.68	0.58	1.08	0.92	0.86	0.68	0.95
Modulation Index	I_CM, avg Power Factor (PF)			I_DM, avg Power Factor (PF)			I_CM, RMS Power Factor (PF)			I_DM,rms Power Factor (PF)		
	0.5	0.707	0.9	0.5	0.707	0.9	0.5	0.707	0.9	0.5	0.707	0.9
0.4	0.45	0.63	0.85	0.68	0.7	1.02	0.91	0.78	0.88	0.65	0.94	0.74
0.6	1.06	0.95	0.84	0.72	0.95	0.66	1.01	0.88	0.81	069	0.72	0.93
0.8	1.06	0.82	0.79	0.58	0.68	0.84	0.96	1.05	0.78	0.9	0.84	0.68
0.95	0.87	1.1	0.96	0.89	0.55	0.78	0.68	0.95	1.08	0.73	0.59	0.79
Modulation Index	I_CTB, avg Power Factor (PF)			I_DTB, avg Power Factor (PF)			I_CTB, rms Power Factor (PF)			I_DTB,rms Power Factor (PF)		
	0.5	0.707	0.9	0.5	0.707	0.9	0.5	0.707	0.9	0.5	0.707	0.9
0.4	1.02	0.87	0.95	0.56	0.87	0.55	0.98	0.92	0.76	0.84	0.94	0.55
0.6	0.86	1.09	0.99	0.82	0.68	0.96	0.76	0.83	0.57	1.06	0.96	0.58
0.8	1.02	0.66	0.98	0.92	0.76	0.81	0.98	0.75	0.62	0.81	1.1	0.87
0.95	0.69	0.78	0.59	0.71	0.92	0.86	0.74	1.06	0.98	0.75	0.69	0.85

current is assumed 1.5 kA for all modulation indices and various PFs. So, the load impedance is not considered constant.

According to the derived analytical equations as well as simulation results in Figs. 5–7, it is worth mentioning that by increasing the modulation index, the average, and RMS currents of the high-frequency IGBTs, top/bottom low-frequency IGBTs/diodes increase whereas the average and RMS currents of high-frequency antiparallel diodes, middle low-frequency IGBTs/diodes decrease. In addition, average and RMS currents of all low-frequency antiparallel diodes are negligible as compared to high-frequency antiparallel diodes, and this fact is significant for high PFs. It is noteworthy of mentioning that middle low-frequency antiparallel diodes have higher values of average and RMS currents in comparison with top/bottom low-frequency antiparallel diodes. Additionally, the average and RMS current of all IGBTs are higher than average and RMS current of antiparallel diodes.

TABLE V
ERROR (%) BETWEEN THE NUMERICAL COMPUTATIONS RESULTS AND EXPERIMENTAL MEASUREMENTS OF THE AVERAGE AND RMS CURRENTS OF IGBTS AND DIODES IN THE 1.5-KW FIVE-LEVEL SINGLE-PHASE ANPC-FCM CONVERTER

PF	0.26	0.48	0.63	0.73	0.82	0.9
$I_{CHF,avg}$	2.52 (1.67)	2.47 (1.69)	2.29 (1.72)	2.07 1.75)	1.79 (1.81)	1.40 (1.91)
$I_{DHF,avg}$	2.02 (1.24)	1.65 (1.28)	1.34 (1.24)	1.10 (1.85)	0.88 (1.75)	0.63 (1.71)
$I_{CTB,avg}$	1.48 (1.27)	1.74 (1.14)	1.80 (1.76)	1.75 (1.49)	1.60 (2.07)	1.31 (1.24)
$I_{DTB,avg}$	0.63 (2.39)	0.33 (2.23)	0.17 (2.68)	0.09 (2.69)	0.04 (2.35)	0.01 (2.75)
$I_{CM,avg}$	1.39 (1.34)	1.31 (1.56)	1.16 (1.34)	1.01 (1.18)	0.84 (1.85)	0.62 (1.61)
$I_{DM,avg}$	1.03 (1.17)	0.73 (1.38)	0.49 (2.16)	0.32 (1.95)	0.19 (1.25)	0.08 (1.56)
$I_{CHF,rms}$	5.22 (1.29)	4.91 (1.23)	4.46 (1.88)	3.99 (1.45)	3.45 (1.38)	2.69 (1.92)
$I_{DHF,rms}$	4.86 (1.96)	4.24 (1.57)	3.57 (1.53)	2.98 (1.86)	2.41 (1.52)	1.73 (1.94)
$I_{CTB,rms}$	3.94 (1.67)	4.20 (2.18)	4.08 (1.95)	3.79 (2.14)	3.35 (2.35)	2.66 (2.53)
$I_{DTB,rms}$	2.29 (2.27)	1.47 (2.48)	0.91 (2.34)	0.56 (2.25)	0.32 (2.83)	0.13 (2.77)
$I_{CM,rms}$	4.29 (2.14)	3.97 (1.55)	3.45 (1.41)	2.93 (1.15)	2.39 (1.41)	1.72 (1.26)
$I_{DM,rms}$	3.42 (2.91)	2.55 (2.64)	1.80 (2.22)	1.25 (2.25)	0.82 (2.54)	0.41 (2.12)

B. Validation Through Experimental Measurements

In this section, a laboratory-scale converter of a 1.5-kW five-level single-phase ANPC-FCM converter is built in order to make a comparative analysis between numerical computation results and measured experimental results. The dc link voltage for the ANPC-FCM converter is 600 V and utilized IGBTs and ultrafast diodes are IXGH48N60B3 and RURP3060, respectively. The TMS320F28335 DSP manufactured by Texas Instruments has been used to modulate the ANPC-FCM converter. The gate driver ICs for IGBTs are IR2184 with gate resistance of $R_G = 10\ \Omega$. The DCP021515 IC is used to provide required isolated dc voltages for gate drive circuitry of IGBT modules. To validate the derived closed-form solutions for the analytic computation of RMS and average currents flowing through IGBTs and antiparallel diodes, experimental tests are conducted for different load PFs. The analytic results and the associated errors expressed in percentage (numbers in parenthesis) between numerical computation results and experimental measurements for each case are listed in Table V while demonstrating a good accuracy for derived closed-form equations. For experimental measurements, the converter modulation index (M) is set at 0.9 whereas load PF varies from 0.26 to 0.90 (six different cases). At PF of 0.9, the resistive–inductive load is $R = 38\ \Omega$ and $L = 58\ \mathrm{mH}$. For the rest of the experiments, the load inductance is kept constant while the resistance is changed to attain the required PFs mentioned in the test. In Table V, all notations of the switches and diodes are based on Fig. 2. As it is obvious, the maximum error is roughly 3% which sounds reasonable and acceptable for experimental verification. The obtained errors can be due to the miscalculation in the oscilloscope computation,

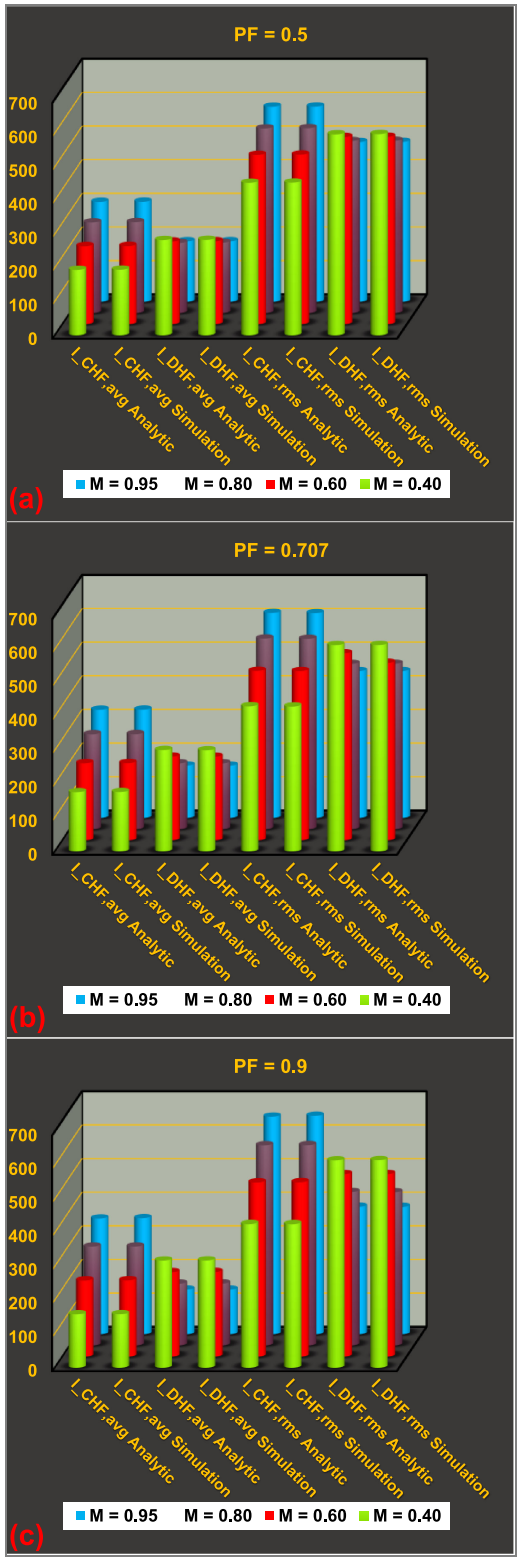

Fig. 5. Comparison between numerical computation and simulation results of the average and RMS currents [A] of the high-frequency IGBTs and diodes in a 12.1-MVA 6.6-kV nine-level (line-to-line) ANPC-FCM converter for PFs of: (a) 0.5. (b) 0.707. (c) 0.9.

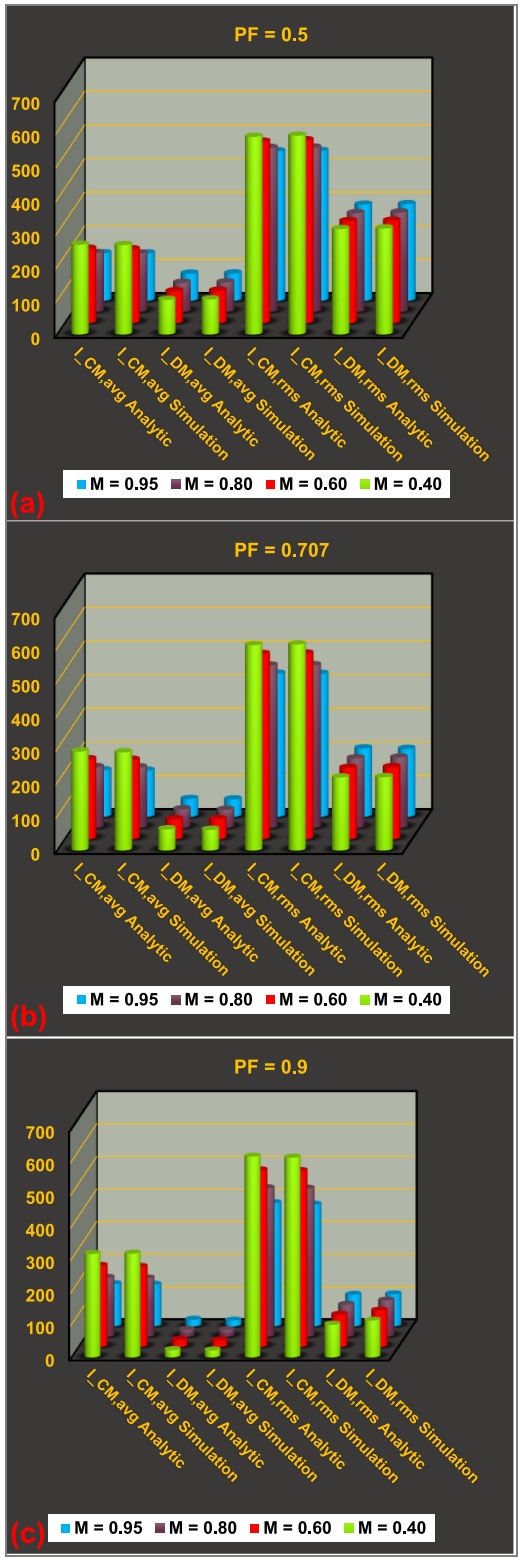

Fig. 6. Comparison between numerical computation and simulation results of the average and RMS currents [A] of the middle low-frequency IGBTs and diodes in a 12.1-MVA 6.6-kV nine-level (line-to-line) ANPC-FCM converter for PFs of: (a) 0.5. (b) 0.707. (c) 0.9.

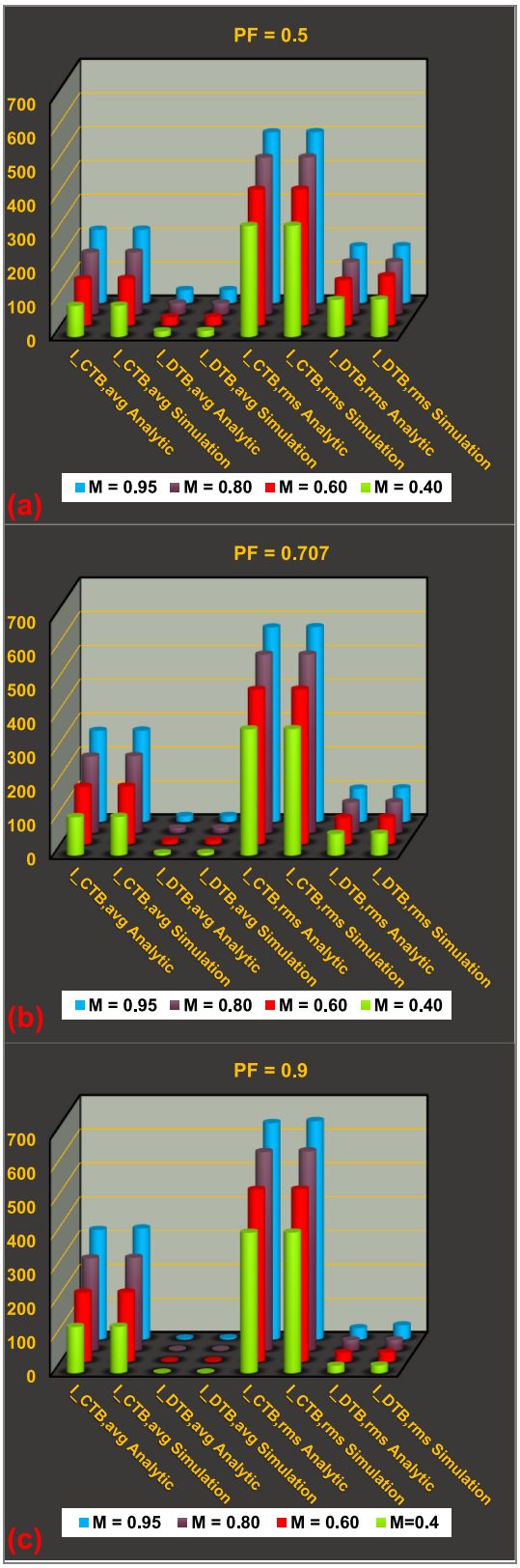

Fig. 7. Comparison between numerical computation and simulation results of the average and RMS currents [A] of the top/bottom low-frequency IGBTs and diodes in a 12.1-MVA 6.6-kV nine-level (line-to-line) ANPC-FCM converter for PFs of: (a) 0.5. (b) 0.707. (c) 0.9.

variation of the load impedance under test, and/or interference of the noise with current probe measured values.

V. Conduction Power Loss Investigation in the ANPC-FCM Converter

After verifying the derived equations to calculate the average and RMS current of IGBTs and diodes in ANPC-FCM converter through simulation and experimental results, these closed-from equations are utilized to calculate the conduction power losses of IGBTs, diodes, and switching-power-cells as well as the whole three-phase ANPC-FCM converter. The obtained results as a function of converter modulation index and load PF for a 12.1-MVA 6.6-kV nine-level (line-to-line) ANPC-FCM converter are shown in various cases in Figs. 8–12.

In Figs. 8 and 9, the load impedance $(|Z| = \sqrt{(R^2 + (L\omega)^2)} = 3.6\ \Omega)$ is considered constant; hence, its current varies linearly with converter modulation index while load peak current in Figs. 10–12 is considered constant. It can be pointed out from Fig. 9 that by increasing the converter modulation index the conduction power loss of all IGBTs and antiparallel diodes increase. Moreover, it can be concluded that by increasing load PF, conduction power loss of high-frequency and top/bottom low-frequency IGBTs increase whereas increasing load PF decreases conduction power losses in high-frequency and top/bottom low-frequency antiparallel diodes. The same phenomenon occurs in the middle low-frequency IGBTs and antiparallel diodes. According to Fig. 9, it is worth mentioning that increasing load PF does not have a significant impact on the conduction power loss in both of the high and low-frequency switching-power-cells. Herein, one high-frequency switching-power-cell contains two complementary high-frequency IGBTs and their antiparallel diodes, and the low-frequency switching-power-cell (which is only one) contains all low-frequency IGBTs and their antiparallel diodes. As mentioned previously, each low-frequency IGBT is series connection of two IGBTs since IGBTs in low-frequency power cell need to withstand the voltage two times of blocking voltage of IGBTs in high-frequency power cell. Therefore, each low-frequency power cell contains eight IGBTs and their anti-parallel diodes while high-frequency power cell contains two IGBTs and their anti-parallel diodes. Hence, it is expected that each low-frequency power cell has conduction power loss four times higher than power loss of high-frequency power cell. However, Fig. 9 shows interestingly that each low-frequency power cell has conduction power loss almost two times of power loss of high-frequency power cell. The reason is that low-frequency anti-parallel diodes have negligible power loss while high-frequency anti-parallel diodes have significant power loss as shown in Fig. 8.

Cell components' conduction power loss versus modulation index and PF in a 12.1-MVA 6.6-kV ANPC-FCM converter considering constant load current are depicted in Figs. 10–12. Based on Figs. 10–12, the low-frequency IGBTs and switching-power-cells possess more conduction losses as compared to the high-frequency IGBTs and power-cells. According to Fig. 12(c), the maximum conduction power loss of 12.1-MVA 6.6-kV three-phase nine-level ANPC-FCM occurs for almost purely resistive load and its value is around 38.55 kW. Even though this amount

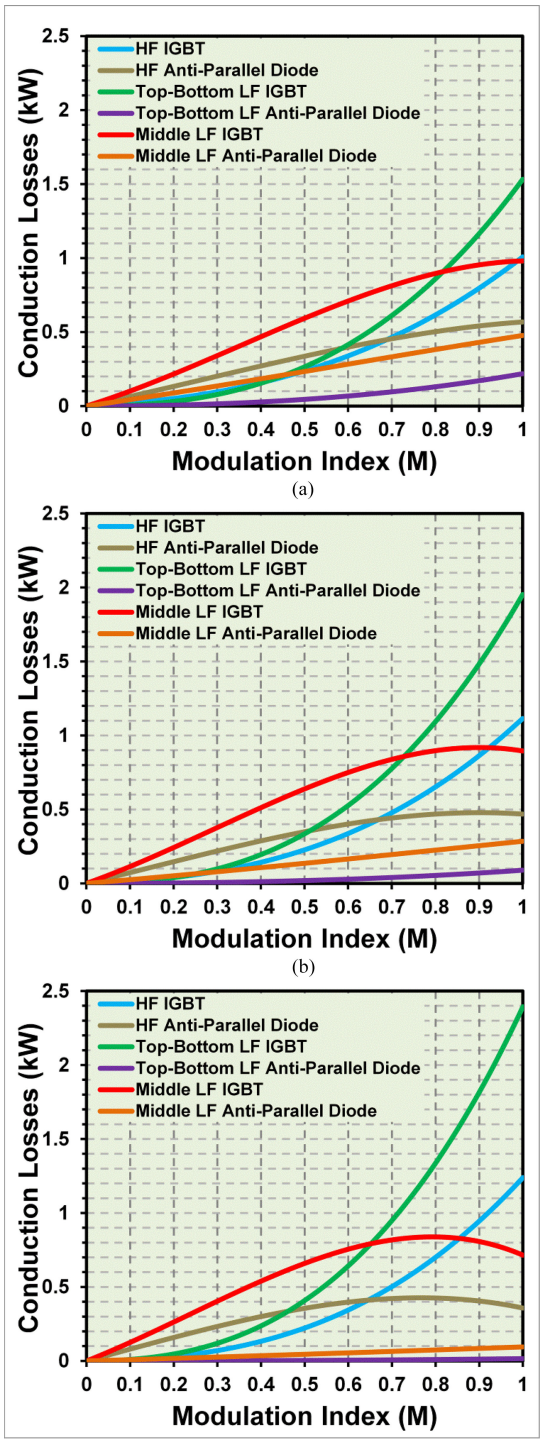

Fig. 8. High-frequency and low-frequency IGBTs/diodes power loss versus modulation index in a 12.1-MVA 6.6-kV 9-level (line-to-line) ANPC-FCM converter considering constant load impedance for load PFs of: (a) 0.5. (b) 0.707. (c) 0.9.

of power loss produces a lot of heat and its dissipation needs significant heat sink with advanced cooling system (i.e., water cooling system), this is low as compared to the converter output power which is 12.1 MVA. In other words, total conduction power loss of the converter is 0.318% of the output power.

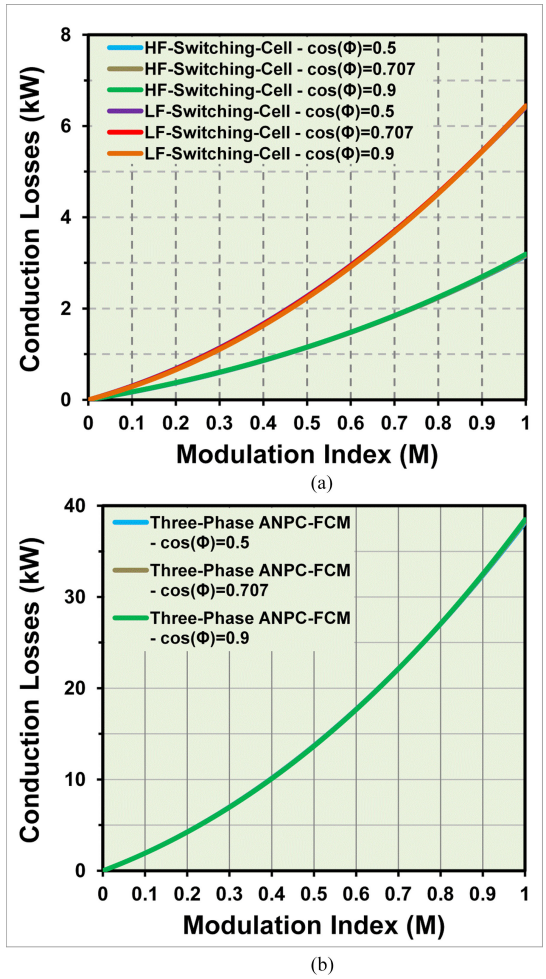

Fig. 9. Conduction power loss versus modulation index in a 12.1-MVA 6.6-kV nine-level (line-to-line) ANPC-FCM converter considering constant load impedance: (a) conduction power loss of high-frequency and low-frequency power cells; (b) total conduction power loss of three-phase ANPC-FCM converter.

VI. Analytical Determination of Switching Power Losses in ANPC-FCM Converters Using Kapteyn (Fourier-Bessel) Series

Power loss in an IGBT or diode originates from two sources. The first source which is discussed in detail in previous sections is the conduction power loss as current flows through the semiconductor devices. The other source of the power loss is through switching losses which are generated due to switching delays that are intrinsic to the semiconductor device. During the turn-on and turn-off switching processes, voltage and current do not instantaneously change. Subsequently, both of them can simultaneously have significant values, and their product (power) can reach very high values. Moreover, the intrinsic parasitic capacitance of the semiconductor device stores, and then, dissipates energy during each switching transition. Therefore, as a semiconductor device turns on and off, it dissipates energy during each switching transition. These processes last only for short periods of time, although they occur repetitively several times within a second. For this reason, switching losses are directly proportional to the switching frequency. In addition, the

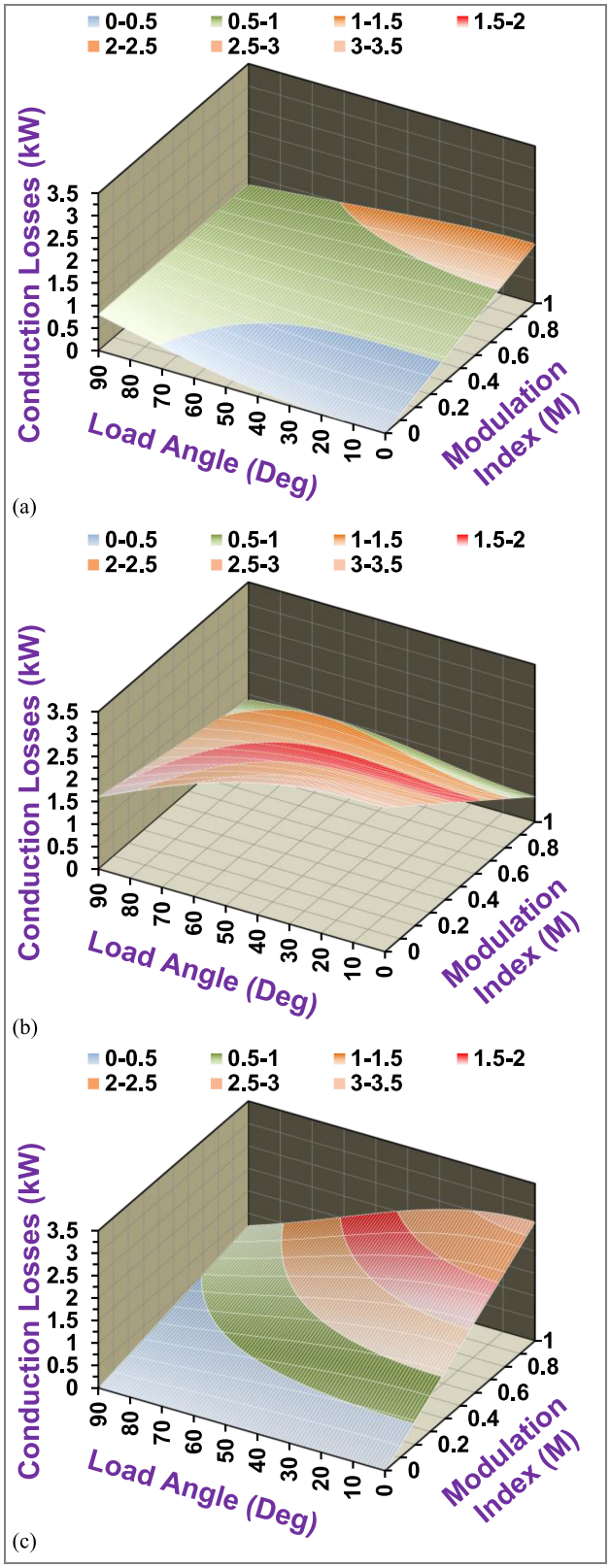

Fig. 10. Cell components' conduction power loss versus modulation index and PF in a 12.1-MVA 6.6-kV nine-level (line-to-line) ANPC-FCM converter considering constant load current (Ip = 1500 A): (a) high-frequency IGBT conduction power loss (b) middle low-frequency IGBT conduction power loss (c) top/bottom low-frequency IGBT conduction power loss.

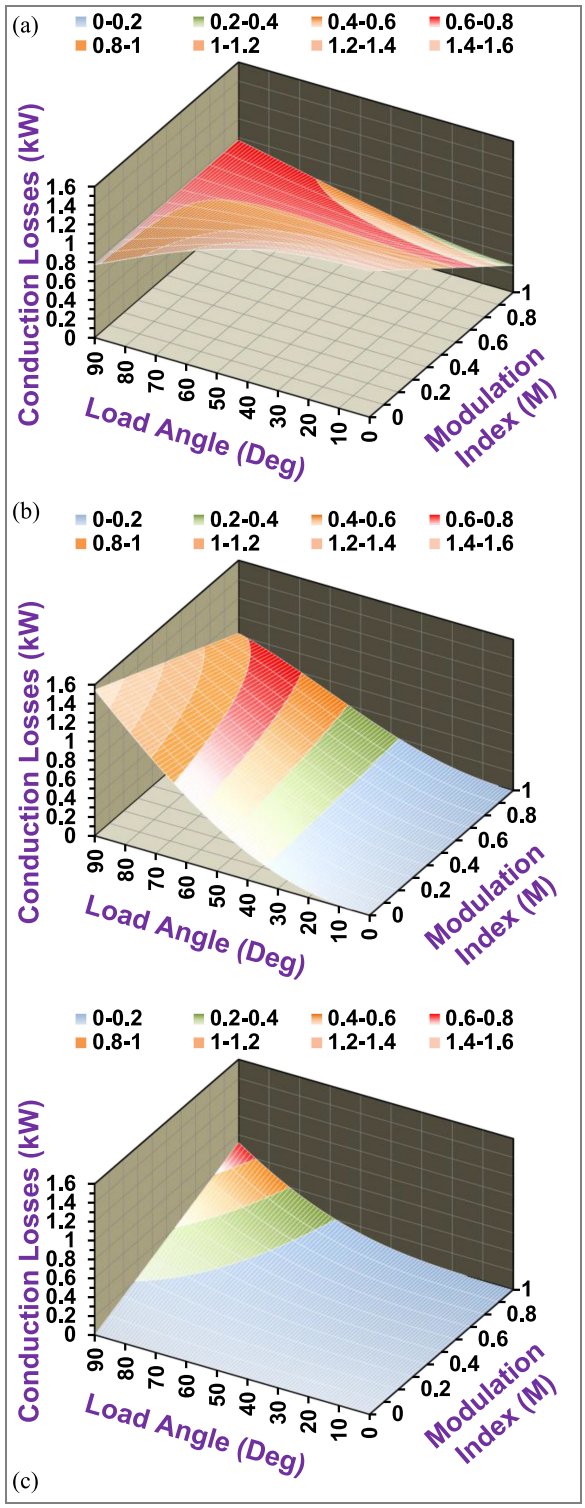

Fig. 11. Cell components' conduction power loss versus modulation index and PF in a 12.1-MVA 6.6-kV 9-level (line-to-line) ANPC-FCM converter considering constant load current (Ip = 1500 A): (a) high-frequency anti-parallel diode conduction power loss, (b) middle low-frequency antiparallel diode conduction power loss, (c) top/bottom low-frequency antiparallel diode conduction power loss.

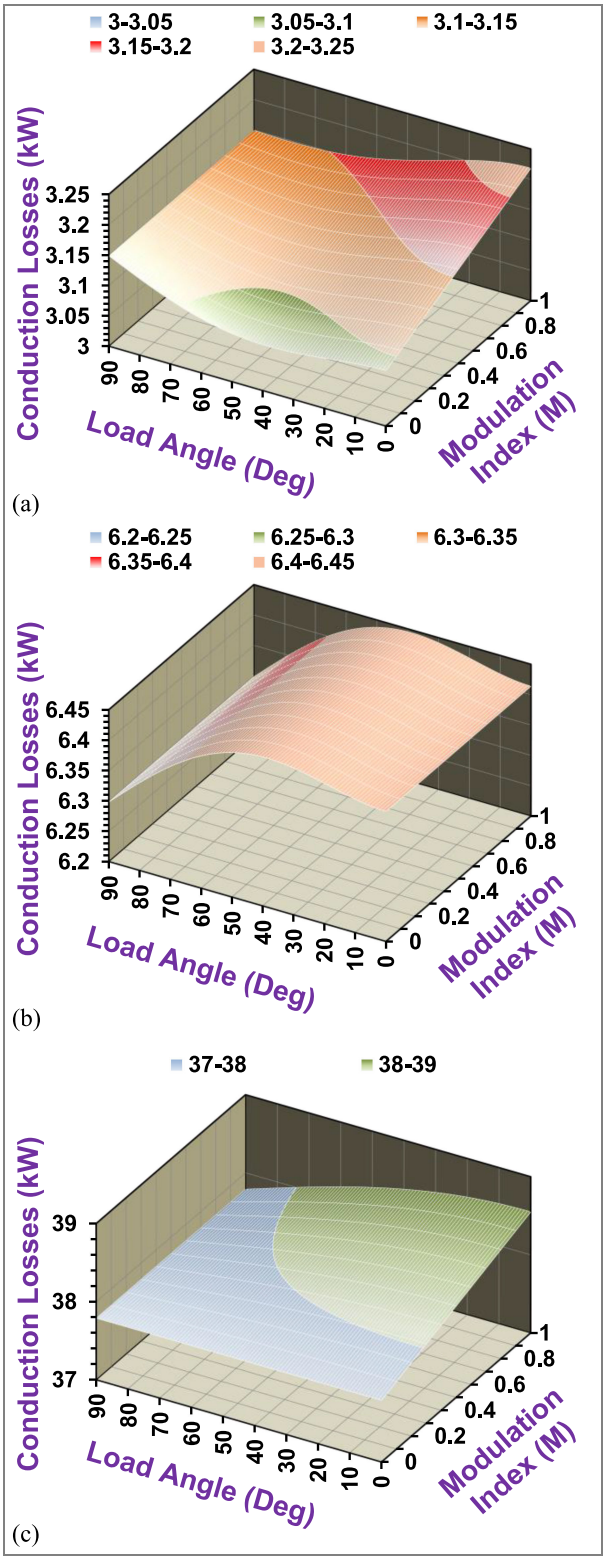

Fig. 12. Cell components' conduction power loss versus modulation index and PF in a 12.1-MVA 6.6-kV nine-level (line-to-line) ANPC-FCM converter considering constant load current (Ip = 1500 A): (a) one high-frequency switching-power-cell conduction loss, (b) one low-frequency switching-power-cell conduction loss, (c) total conduction power loss of a three-phase ANPC-FCM converter.

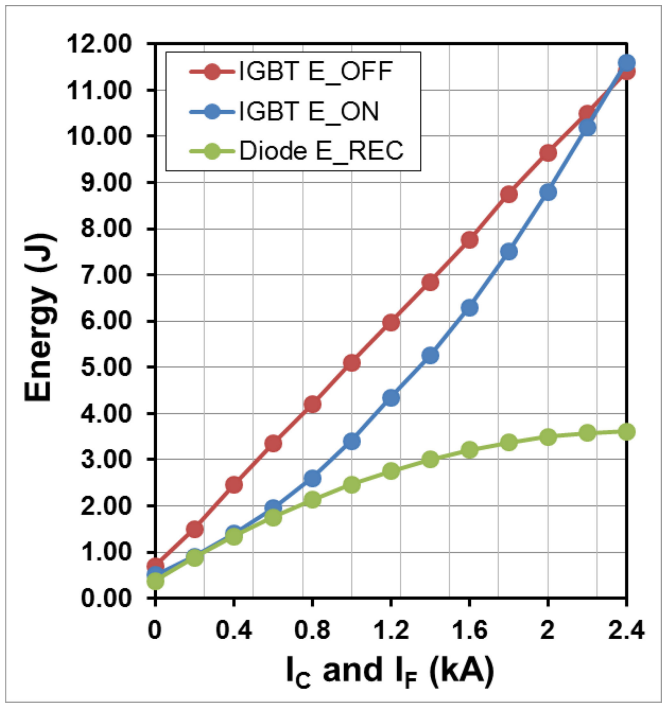

Fig. 13. Energy loss of IGBT turn on/off and diode reverse recovery in ABB 5SNA 1200G450300 HiPak 4.5-kV 1.2-kA IGBT module.

switching power loss is also proportional to the value of the blocked voltage across the semiconductor device, i.e., off-state voltage, [51]–[57]. Both turn-on loss ($E_{\rm ON}$) and turn-off loss ($E_{\rm OFF}$) of the IGBT should be considered. However, only reverse recovery loss ($E_{\rm REC}$) during turn off should be considered for diode since its turn-on loss is negligible and even datasheets do not provide this data [51]–[58]. The formula for calculation of the switching losses in the IGBT and diode can be expressed as follows:

$$P_{\rm SWT} = \frac{1}{T}\frac{V_{\rm CE}}{V_{\rm CE\_ref}}\sum_{j=1}^{j=\frac{f_{\rm sw}}{f}}\left(E_{{\rm ON}_j}(I_C)+E_{{\rm OFF}_j}(I_C)\right) \tag{44}$$

$$P_{\rm SWD} = \frac{1}{T}\frac{V_F}{V_{F\_\rm ref}}\sum_{j=1}^{j=\frac{f_{\rm sw}}{f}}\left(E_{{\rm REC}_j}(I_D)\right) \tag{45}$$

where $P_{\rm SWT}$ and $P_{\rm SWD}$ are the switching power loss of the IGBT and diode, respectively, I_C and I_D are the current flowing through the IGBT and diode at switching instant, respectively, $f_{\rm SW}$ is the switching frequency, T and f are fundamental period and frequency, respectively, $V_{\rm CE\_ref}$ and $V_{F\_\rm ref}$ are the blocking voltage from datasheet which equal to 2.8 kV, and $V_{\rm CE}$ and V_F are the blocking voltage in the performed analytical analysis and equal to 2.7 kV. Fig. 13 depicts the switching energy of IGBT and diode ($E_{\rm ON}$, $E_{\rm OFF}$, and $E_{\rm REC}$) versus their current at ON/OFF switching moments. These data are obtained from the datasheet of ABB 5SNA 1200G450300 HiPak 4.5-kV 1.2-kA IGBT module at the junction temperature of 125 °C while $V_{\rm CE\_ref}$ equals 2.8 kV.

TABLE VI
SECOND-ORDER APPROXIMATION OF IGBT 5SNA 1200G450300 SWITCHING ENERGY LOSSES

IGBT Turn-on Energy Loss	$E_{\mathrm{on}}(I_C) = 0.515 + 0.0017 \times I_C + 1.2375 \times 10^{-6} \times \mathrm{I}_C^2$
IGBT Turn-off Energy Loss	$E_{\mathrm{off}}(I_C) = 0.6752 + 0.0044 \times \mathrm{I}_C + 4.1583 \times 10^{-8} \times \mathrm{I}_C^2$
Diode Reverse Recovery Energy Loss	$E_{RR}(\mathrm{I}_D) = 0.375 + 0.00261 \times \mathrm{I}_D - 5.25 \times 10^{-7} \times \mathrm{I}_D^2$

Herein, the data depicted in Fig. 13 are used to investigate the switching power loss in 12.1-MVA 6.6-kV three-phase nine-level (line-to-line) ANPC-FCM converter. At each switching transition of IGBT and diode, the current before the moment of turn-off transition and after turn-on transition is calculated based on the data of Fig. 13 to compute the switching power loss of IGBT and diode. Energy loss related to IGBT turn on and turn off and reverse recovery of diode can be approximated well with second-order polynomials. It is worth mentioning that these approximations and polynomial equations might be provided by the power switch manufacturer in datasheet. For instance, the second-order approximation of ABB 5SNA 1200G450300 HiPak 4.5-kV 1.2-kA IGBT module switching energy losses depicted in Fig. 13, is illustrated in Table VI.

In order to derive closed-form equations for switching power losses, it is requisite to derive closed-form analytic equations for unknown switching instants of the PWM modulator. After deriving closed-from equations for PWM instants (turn-on and turn-off moments of IGBT and antiparallel diode), it is possible to exploit these PWM instants in switching energy loss equations of the power switch to calculate the switching losses. Hence, the basis of obtaining of the closed-from equations for calculation of the switching power losses is the computation of the switching instants of the PWM modulator.

One of the powerful and standard approaches with a revealed wealth of applications in mathematics, physics, and engineering is to expand an arbitrary analytic function into a series of the specific type, such as the theory of Taylor, Fourier, Neumann, and Kapteyn series. In particular, Kapteyn series have been the object of intense investigations owing to the fact that they are an enabling method in obtaining explicit solutions for implicit equations requiring numeric computations such as Kepler's transcendental equation. Series of the form [59] and [60]

$$f(x) = \sum_{\wp=0}^{+\infty} \left(a_\wp(f)\, J_\wp(\wp x)\right) \tag{46}$$

are the Kapteyn series of the first kind which involve a summation over terms containing one Bessel function of the form $J_\wp(\wp x)$ where $a_\wp(f)$ are coefficients depending on $f(x)$. Kapteyn series made, indeed, their first appearance in solution of Kepler's problem. The solution of the Kepler's transcendental equation

$$E - \varepsilon \sin(E) = M \tag{47}$$

in terms of Kapteyn series yields [59]

$$E = M + \sum_{\wp=1}^{+\infty} \left(\frac{2}{\wp} \sin(\wp M)\, J_\wp(\wp\varepsilon)\right). \tag{48}$$

The relevance of Kapteyn series to the spectral analysis of PWM modulated systems is well examined in [59], on the basis of isomorphism between the implicit equation of the unknown PWM instants and Kepler's problem concerning elliptic motion under inverse square law.

According to switching pattern of ANPC-FCM converters, the triangular carrier waveform can be defined as follows:

$$\Omega(t) = \begin{cases} E_c\left(\frac{2}{T_c}t - 2q\right) & qT_c \le t \le qT_c + \frac{T_c}{2} \\ -E_c\left(\frac{2}{T_c}t - 2q - 2\right) & qT_c + \frac{T_c}{2} \le t \le (q+1)T_c \end{cases}$$
$$q \in \mathbb{Z}^+ \tag{49}$$

where, $f_c = 1/T_c$, and E_c are the triangular carrier waveform frequency (f_{SW}) and amplitude, respectively. By intersection of triangular carrier waveform with sinusoidal reference waveform with amplitude of E_m and frequency of $f_r = f_c/k = 1/kT_c$, the switching instants of the modulator can be obtained. To determine the switching instants resulted from intersection of the rising side of the triangular carrier waveform with sinusoidal reference waveform during first half-cycle ($0 \le \omega t \le \pi$), following equation should be solved:

$$E_m \sin(\omega_r \alpha_{1q}) = E_c\left(\frac{2}{T_c}\alpha_{1q} - 2q\right). \tag{50}$$

Equation (50) can be rearranged as follows:

$$E_{1q} - \varepsilon \sin(E_{1q}) = M_{1q} \tag{51}$$

where the following notations are used:

$$\begin{aligned} E_{1q} &= \frac{2\pi}{kT_c}\alpha_{1q} \\ M_{1q} &= \frac{2\pi q}{k} \\ \omega_r &= \frac{2\pi}{kT_c} \\ \varepsilon &= \frac{\pi E_m}{kE_c}. \end{aligned} \tag{52}$$

The aforesaid isomorphism between Kepler's transcendental equation and (50) is so obvious in the form of (51). Hence, the analytic solution of (50) in terms of Kapteyn series yields as follows:

$$\alpha_{1q} = qT_c + \sum_{\wp=1}^{+\infty} \left(\frac{2}{\wp\omega_r} \sin(\wp q \omega_r T_c)\, J_\wp(\wp\varepsilon)\right). \tag{53}$$

For the falling side of the triangular carrier waveform in the similar procedure, we can write

$$E_m \sin(\omega_r \alpha_{2q}) = -E_c\left(\frac{2}{T_c}t - 2q - 2\right). \tag{54}$$

The solution of (54) in terms of Kapteyn series yields as follows:

$$\alpha_{2q} = (q+1)T_c + \sum_{\wp=1}^{+\infty} \left(\frac{2(-1)^\wp}{\wp\omega_r} \sin(\wp(q+1)\omega_r T_c)\, J_\wp(\wp\varepsilon)\right). \tag{55}$$

PWM switching instants for second half-cycle ($\pi \leq \omega t \leq 2\pi$), can be derived as follows:

$$\beta_{1q} = \left(q + \frac{1}{2E_c}\right) T_c + \sum_{\wp=1}^{+\infty} \left(\frac{2}{\wp\omega_r} J_\wp(\wp\varepsilon) \sin\left(\wp\left(q\omega_r T_c + \frac{\varepsilon}{E_m}\right)\right)\right) \quad (56)$$

$$\beta_{2q} = \left(q+1-\frac{1}{2E_c}\right) T_c + \sum_{\wp=1}^{+\infty} \left(\frac{2(-1)^\wp}{\wp\omega_r} \sin\left(\wp\left((q+1)\omega_r T_c - \frac{\varepsilon}{E_m}\right)\right) J_\wp(\wp\varepsilon)\right). \quad (57)$$

After deriving analytic solutions for PWM switching instants, it is necessary to derive natural commutation instant of current between IGBT and antiparallel diode and the corresponding q according to load PF as follows wherein [] is a floor function:

$$\alpha_N = \frac{\cos^{-1}(\mathrm{PF})}{2\pi f_r} = \frac{\theta}{2\pi f_r} \quad (58)$$

$$q' = \left[\frac{\alpha_N}{T_c}\right] = \left[k\frac{\cos^{-1}(\mathrm{PF})}{2\pi}\right] = \left[\frac{k\theta}{2\pi}\right] \quad (59)$$

$$\beta_N = \frac{\pi + \cos^{-1}(\mathrm{PF})}{2\pi f_r} = \frac{\pi+\theta}{2\pi f_r} \quad (60)$$

$$q'' = \left[\frac{\beta_N}{T_c}\right] = \left[k\frac{\pi + \cos^{-1}(\mathrm{PF})}{2\pi}\right] = \left[k\frac{\pi+\theta}{2\pi}\right]. \quad (61)$$

According to natural commutation instants, following three scenarios can be considered for PWM switching instants:

$$\text{Scenario I} = \begin{cases} q'T_c \leq \alpha_N \leq \alpha_{1q'} \\ q''T_c \leq \beta_N \leq \beta_{1q''} \end{cases} \quad (62)$$

$$\text{Scenario II} = \begin{cases} \alpha_{1q'} \leq \alpha_N \leq \alpha_{2q'} \\ \beta_{1q''} \leq \beta_N \leq \beta_{2q''} \end{cases} \quad (63)$$

$$\text{Scenario III} = \begin{cases} \alpha_{2q'} \leq \alpha_N \leq (q'+1)T_c \\ \beta_{2q''} \leq \beta_N \leq (q''+1)T_c \end{cases}. \quad (64)$$

A. Analytical Determination of Switching Power Losses for High-frequency IGBTs and Diodes for Scenario I

Switching energy loss for one high-frequency antiparallel diode (reverse recovery energy loss) according to PWM instants can be obtained as follows:

$$E_{\mathrm{RR,HF,Diode}} = \sum_{q=0}^{q'-1} E_{\mathrm{RR}}\left(-I_p \sin(\omega_r\alpha_{1q} - \theta)\right) + \sum_{q=q''}^{k-1} E_{\mathrm{RR}}\left(-I_p \sin(\omega_r\beta_{1q} - \theta)\right). \quad (65)$$

Turn-on and turn-off energy losses of one high-frequency IGBT for even values of k can be calculated as follows:

$$E_{\mathrm{on,HF,IGBT}} = \sum_{q=q'}^{\frac{k}{2}-1} E_{\mathrm{on}}\left(I_p \sin(\omega_r\alpha_{2q} - \theta)\right) + \sum_{q=\frac{k}{2}}^{q''-1} E_{\mathrm{on}}\left(I_p \sin(\omega_r\beta_{2q} - \theta)\right) \quad (66)$$

$$E_{\mathrm{off,HF,IGBT}} = \sum_{q=q'}^{\frac{k}{2}-1} E_{\mathrm{off}}\left(I_p \sin(\omega_r\alpha_{1q} - \theta)\right) + \sum_{q=\frac{k}{2}}^{q''-1} E_{\mathrm{off}}\left(I_p \sin(\omega_r\beta_{1q} - \theta)\right). \quad (67)$$

Turn-on and turn-off energy losses of one high-frequency IGBT for odd values of k can be calculated as follows:

$$E_{\mathrm{on,HF,IGBT}} = \sum_{q=q'}^{\left[\frac{k}{2}\right]-1} E_{\mathrm{on}}\left(I_p \sin(\omega_r\alpha_{2q} - \theta)\right) + \sum_{q=\left[\frac{k}{2}\right]}^{q''-1} E_{\mathrm{on}}\left(I_p \sin(\omega_r\beta_{2q} - \theta)\right) \quad (68)$$

$$E_{\mathrm{off,HF,IGBT}} = \sum_{q=q'}^{\left[\frac{k}{2}\right]} E_{\mathrm{off}}\left(I_p \sin(\omega_r\alpha_{1q} - \theta)\right) + \sum_{q=\left[\frac{k}{2}\right]+1}^{q''-1} E_{\mathrm{off}}\left(I_p \sin(\omega_r\beta_{1q} - \theta)\right). \quad (69)$$

B. Analytical Determination of Switching Power Losses for High-Frequency IGBTs and Diodes for Scenario II

Switching energy loss for one high-frequency antiparallel diode (reverse recovery energy loss) according to PWM instants can be obtained as follows:

$$E_{\mathrm{RR,HF,Diode}} = \sum_{q=0}^{q'} E_{\mathrm{RR}}\left(-I_p \sin(\omega_r\alpha_{1q} - \theta)\right) + \sum_{q=q''+1}^{k-1} E_{\mathrm{RR}}\left(-I_p \sin(\omega_r\beta_{1q} - \theta)\right). \quad (70)$$

Turn-on and turn-off energy losses of one high-frequency IGBT for even values of k can be calculated as follows:

$$E_{on,\mathrm{HF,IGBT}} = \sum_{q=q'}^{\frac{k}{2}-1} E_{\mathrm{on}}\left(I_p \sin\left(\omega_r \alpha_{2q} - \theta\right)\right) + \sum_{q=\frac{k}{2}}^{q''-1} E_{\mathrm{on}}\left(I_p \sin\left(\omega_r \beta_{2q} - \theta\right)\right) \quad (71)$$

$$E_{\mathrm{off,HF,IGBT}} = \sum_{q=q'+1}^{\frac{k}{2}-1} E_{\mathrm{off}}\left(I_p \sin\left(\omega_r \alpha_{1q} - \theta\right)\right) + \sum_{q=\frac{k}{2}}^{q''} E_{off}\left(I_p \sin\left(\omega_r \beta_{1q} - \theta\right)\right). \quad (72)$$

Turn-on and turn-off energy losses of one high-frequency IGBT for odd values of k can be calculated as follows:

$$E_{on,\mathrm{HF},IGBT} = \sum_{q=q'}^{\left[\frac{k}{2}\right]-1} E_{on}\left(I_p \sin\left(\omega_r \alpha_{2q} - \theta\right)\right) + \sum_{q=\left[\frac{k}{2}\right]}^{q''-1} E_{on}\left(I_p \sin\left(\omega_r \beta_{2q} - \theta\right)\right) \quad (73)$$

$$E_{off,\mathrm{HF},IGBT} = \sum_{q=q'+1}^{\left[\frac{k}{2}\right]} E_{off}\left(I_p \sin\left(\omega_r \alpha_{1q} - \theta\right)\right) + \sum_{q=\left[\frac{k}{2}\right]+1}^{q''} E_{off}\left(I_p \sin\left(\omega_r \beta_{1q} - \theta\right)\right). \quad (74)$$

C. Analytical Determination of Switching Power Losses for High-Frequency IGBTs and Diodes for Scenario III

Switching energy loss for one high-frequency antiparallel diode (reverse recovery energy loss) according to PWM instants can be obtained as follows:

$$E_{\mathrm{RR},HF,Diode} = \sum_{q=0}^{q'} E_{\mathrm{RR}}\left(-I_p \sin\left(\omega_r \alpha_{1q} - \theta\right)\right) + \sum_{q=q''+1}^{k-1} E_{\mathrm{RR}}\left(-I_p \sin\left(\omega_r \beta_{1q} - \theta\right)\right). \quad (75)$$

Turn-on and turn-off energy losses of one high-frequency IGBT for even values of k can be calculated as follows:

$$E_{on,\mathrm{HF},IGBT} = \sum_{q=q'+1}^{\frac{k}{2}-1} E_{on}\left(I_p \sin\left(\omega_r \alpha_{2q} - \theta\right)\right) + \sum_{q=\frac{k}{2}}^{q''} E_{on}\left(I_p \sin\left(\omega_r \beta_{2q} - \theta\right)\right) \quad (76)$$

$$E_{off,\mathrm{HF},IGBT} = \sum_{q=q'+1}^{\frac{k}{2}-1} E_{off}\left(I_p \sin\left(\omega_r \alpha_{1q} - \theta\right)\right) + \sum_{q=\frac{k}{2}}^{q''} E_{\mathrm{off}}\left(I_p \sin\left(\omega_r \beta_{1q} - \theta\right)\right). \quad (77)$$

Turn-on and turn-off energy losses of one high-frequency IGBT for odd values of k can be calculated as follows:

$$E_{on,\mathrm{HF},IGBT} = \sum_{q=q'+1}^{\left[\frac{k}{2}\right]-1} E_{on}\left(I_p \sin\left(\omega_r \alpha_{2q} - \theta\right)\right) + \sum_{q=\left[\frac{k}{2}\right]}^{q''} E_{on}\left(I_p \sin\left(\omega_r \beta_{2q} - \theta\right)\right) \quad (78)$$

$$E_{off,\mathrm{HF},IGBT} = \sum_{q=q'+1}^{\left[\frac{k}{2}\right]} E_{off}\left(I_p \sin\left(\omega_r \alpha_{1q} - \theta\right)\right) + \sum_{q=\left[\frac{k}{2}\right]+1}^{q''} E_{\mathrm{off}}\left(I_p \sin\left(\omega_r \beta_{1q} - \theta\right)\right). \quad (79)$$

After calculation of the switching energy losses, the switching power losses can be obtained as follows:

$$P_{\mathrm{SWT,on,HF}} = \frac{1}{T}\frac{V_{CE}}{V_{CE\_\mathrm{ref}}} E_{\mathrm{on,HF},IGBT} \quad (80)$$

$$P_{\mathrm{SWT,off,HF}} = \frac{1}{T}\frac{V_{\mathrm{CE}}}{V_{\mathrm{CE\_ref}}} E_{\mathrm{off,HF},IGBT} \quad (81)$$

$$P_{\mathrm{SWD,RR,HF}} = \frac{1}{T}\frac{V_F}{V_{F\_\mathrm{ref}}} E_{\mathrm{RR},HF,\mathrm{Diode}}. \quad (82)$$

D. Analytical Determination of Switching Power Losses for Low-Frequency IGBTs and Diodes

Due to low-frequency operation principal of some power switches and diodes in ANPC-FCM multilevel converter, following closed-form equations can be derived for switching

TABLE VII
SWITCHING POWER LOSS [KW] INVESTIGATION USING DERIVED CLOSED-FORM EQUATIONS AND SIMULATION RESULTS FOR 12.1-MVA 6.6-KV NINE-LEVEL (LINE-TO-LINE) ANPC-FCM CONVERTER PER APPLIED SWITCHING SEMICONDUCTOR DEVICES AND THE WHOLE THREE-PHASE CONVERTERS CONSIDERING CONSTANT LOAD CURRENT

Modulation Index & Load Peak Current		M = 0.6 & I_p = 500 A			M = 0.8 & I_p = 1000 A			M = 0.95 & I_p = 1500 A		
Power Factor (Lagging)		0.5	0.707	0.9	0.5	0.707	0.9	0.5	0.707	0.9
Derived Closed Form Equations	High-frequency IGBT	1.1825	1.1901	1.1877	2.0625	2.0776	2.0665	3.0533	3.0819	3.0617
	High-frequency Anti-Parallel Diode	0.4247	0.4068	0.4059	0.6395	0.6297	0.6327	0.7981	0.8013	0.8109
	Low-frequency IGBT	0.1244	0.1075	0.0787	0.2169	0.1829	0.1250	0.3102	0.2588	0.1715
	Three-Phase Converter	20.7787	20.4528	20.0664	35.0266	34.6815	33.8905	49.9404	49.7045	48.5281
Simulation Results	High-frequency IGBT	1.1943	1.2009	1.1972	2.0790	2.0900	2.0810	3.0686	3.1004	3.0770
	High-frequency Anti-Parallel Diode	0.4290	0.4104	0.4091	0.6446	0.6334	0.6372	0.8021	0.8061	0.8149
	Low-frequency IGBT	0.1256	0.1084	0.0793	0.2187	0.1840	0.1259	0.3118	0.2604	0.1723
	Three-Phase Converter	20.9864	20.6369	20.2269	35.3069	34.8895	34.1278	50.1901	50.0027	48.7708

energy and power losses of S_{J2} and S_{J3}:

$$E_{\text{off,LF,IGBT,SJ2}} = E_{off}\left(I_p \sin(\theta)\right) \quad (83)$$

$$E_{\text{off,LF,IGBT,SJ3}} = E_{off}\left(I_p \sin(\theta)\right) \quad (84)$$

$$P_{\text{SWT,off,LF,IGBT,SJ2}} = \frac{1}{T}\frac{V_{CE}}{V_{CE\_\text{ref}}} E_{\text{off,LF,IGBT,SJ2}} \quad (85)$$

$$P_{\text{SWT,off,LF,IGBT,SJ3}} = \frac{1}{T}\frac{V_{\text{CE}}}{V_{\text{CE\_ref}}} E_{\text{off,LF,IGBT,SJ3}}. \quad (86)$$

Note that since the current natural commutation occurs between the antiparallel diodes and IGBTs in low-frequency power switches of S_{J2} and S_{J3}, the antiparallel diodes and IGBTS will not have a reverse recovery energy loss and turn-on energy losses, respectively. In order to verify the derived closed-form equations for calculation of the switching power losses of IGBTs and diodes in the ANPC-FCM converter, numerical computation results of the derived closed-form equations are compared with simulation results. The results are illustrated in Table VII demonstrating an excellent accuracy for derived closed-form equations for calculation of the switching power losses. It is worth mentioning that the switching frequency is 750 Hz, k is 15, and the load is considered as constant load current. The maximum error between analytic calculation of switching losses and simulation results is roughly 2%.

VII. DETERMINATION OF JUNCTION TEMPERATURE FOR IGBTS AND DIODES IN ANPC-FCM CONVERTERS

After calculation of switching power losses utilizing derived closed-form equations, junction temperature and conduction power loss at this junction temperature can be calculated for each semiconductor device as illustrated in Fig. 14. The junction temperature and associated conduction power loss calculation flowchart for each IGBT and diode can be elaborated as following:

1) ANPC-FCM converter parameters such as dc link voltage, converter switching frequency and modulation index, load peak current and PF as well as initial junction temperature for each IGBT and diode must be initialized. In addition, characteristic curves of the embedded IGBTs and diodes are initialized to derive the necessary parameters for calculation of the conduction and switching power losses for each IGBT and diode. These parameters are acquired by polynomial approximation method for each of the utilized semiconductor devices. For instance, turn-on and turn-off energy losses (as depicted in Fig. 13 and approximated in Table VI), thermal coefficients ((9)-(16)), ambient temperature (T_a), thermal impedance of junction to case $(Z_{\text{thermal},j2c})$, and thermal impedance of case to

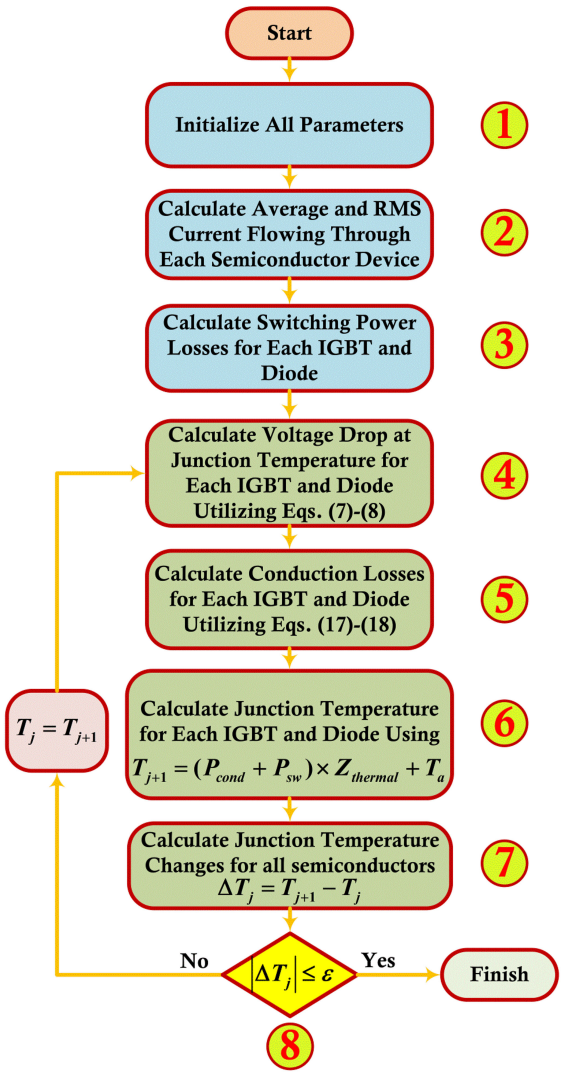

Fig. 14. Junction temperature calculation flowchart for ANPC-FCM converter.

TABLE VIII
JUNCTION TEMPERATURE (C°C, SWITCHING POWER LOSS (KW) , AND CONDUCTION POWER (KW) LOSS CALCULATION USING JUNCTION TEMPERATURE COMPUTATION FLOWCHART FOR IGBTS AND DIODES IN A 12.1-MVA 6.6-KV NINE-LEVEL (LINE-TO-LINE) ANPC-FCM CONVERTER CONSIDERING A CONSTANT IMPEDANCE LOAD

Modulation Index	High-frequency IGBT			Middle Low-frequency IGBT			Top/Bottom Low-frequency IGBT		
	P_{cond}	P_{sw}	T_j	P_{cond}	P_{sw}	T_j	P_{cond}	P_{sw}	T_j
0.4	0.1233 (2.93%)	1.3453 (1.23%)	53.6526 (0.7331%)	0.2076 (3.65%)	0.1225 (1.62%)	31.4407 (0.5934%)	0.0786 (2.46%)	0.1225 (1.96%)	28.9245 (0.2925%)
0.8	0.5866 (2.47%)	2.4612 (1.18%)	84.4631 (1.0055%)	0.3500 (2.83%)	0.2132 (0.86%)	35.9877 (0.6364%)	0.4299 (3.58%)	0.2132 (0.74%)	37.5459 (0.8816%)
0.95	0.9214 (2.64%)	2.9255 (1.23%)	100.0533 (1.1760%)	0.3520 (3.01%)	0.2474 (1.01%)	36.6940 (0.6962%)	0.6747 (3.19%)	0.2474 (1.63%)	42.9894 (1.1597%)
Modulation Index	High-frequency Anti-Parallel Diode			Middle Low-frequency Anti-Parallel Diode			Top/Bottom Low-frequency Anti-Parallel Diode		
	P_{cond}	P_{sw}	T_j	P_{cond}	P_{sw}	T_j	P_{cond}	P_{sw}	T_j
0.4	0.2885 (2.86%)	0.4630 (1.97%)	46.8152 (1.0772%)	0.0555 (3.23%)	0.0181 (0.92%)	26.6121 (0.1957%)	0.0062 (3.34%)	0.0177 (1.84%)	25.1809 (0.0240%)
0.8	0.4514 (3.13%)	0.7079 (1.64%)	58.6549 (1.2739%)	0.1110 (2.97%)	0.0184 (1.43%)	28.2225 (0.3391%)	0.0273 (3.98%)	0.0179 (1.27%)	25.7918 (0.1222%)
0.95	0.4542 (2.97%)	0.7774 (1.53%)	60.7509 (1.2129%)	0.1311 (2.53%)	0.0189 (1.81%)	28.8063 (0.3343%)	0.0397 (3.26%)	0.0187 (1.77%)	26.1528 (0.1437%)

ambient ($Z_{\text{thermal},c2a}$) for each semiconductor is initialized in this stage. It is noteworthy of mentioning that thermal impedance of junction to ambient of each semiconductor is calculated as follows:

$$Z_{\text{thermal},j2a} = Z_{\text{thermal},j2c} + Z_{\text{thermal},c2a}. \tag{87}$$

2) Average and RMS currents flowing through all the IGBTs and diodes are calculated using derived closed-form equations in Section III.
3) Switching power loss is calculated for each IGBT and diode utilizing derived closed-form equations in Section VI.
4) Voltage drops through each IGBT and diode is calculated according to thermal coefficients and junction temperature through (7)–(8).
5) Conduction power loss based on the junction temperature is calculated for each IGBT and diode through (17)–(18).
6) Junction temperature is calculated according to the thermal impedance, conduction loss, switching loss, and the ambient temperature for each IGBT and diode through $T_{j+1} = (P_{\text{cond}} + P_{\text{sw}}) \times Z_{\text{thermal}} + T_a$.
7) Junction temperature changes for each semiconductor ($\Delta T_j = |T_{j+1} - T_j|$) are calculated.
8) Junction temperature changes are compared with a specified accuracy to determine the termination or continuation of the iterative process for calculation of junction temperature.

The process is continued until changes in junction temperature of each IGBT and diode between successive iterations are within a specified accuracy. Using power loss flowchart depicted in Fig. 14, junction temperature is analytically calculated for each IGBT and diodes and compared with simulation results. The results and associated errors are listed in Table VIII. The load peak current is 1.5 kA, load PF is 0.707 (lagging), and load is considered as a constant impedance load, hence the current varies linearly with modulation index. Ambient temperature is 25°C, thermal impedance of case to ambient is 0.01 $\frac{^oC}{W}$, thermal impedance of junction to case for IGBT is 0.0095$\frac{^oC}{W}$ and for diode is 0.019$\frac{^{circ}\text{C}}{\text{W}}$ in 5SNA 1200G450300 HiPak 4.5-kV 1.2-kA IGBT module. The simulation results and the associated error between analytically calculated results and simulation results for each case (numbers in parenthesis) are provided in Table VIII demonstrating a good accuracy for derived closed-form equations.

VIII. CONCLUSION

For appropriate design of multilevel converters, it is of utmost importance and practical interest to evaluate the converter conduction and switching power losses. Investigation of conduction and switching power loss in an ANPC-FCM converter

with any number of switching-power-cells and voltage levels as a function of converter output power, load PF, and modulation index can be very advantageous in the design process. To attain this goal, this paper presented analytical equations for computing RMS and average currents of IGBTs and antiparallel diodes by considering associated duty cycle of each IGBT and antiparallel diode, converter modulation index, load current, and load PF for ANPC-FCM converter. Numerical results of the obtained analytical equations for calculation of RMS and average currents of IGBTs/diodes were compared with simulation and experimental results. The excellent match between analytic, simulation, and experimental results validates derived closed-form equations. Afterward, the obtained equations for RMS and average currents computations were utilized to calculate conduction power loss in a 12.1-MVA 6.6-kV nine-level (line-to-line) ANPC-FCM power converter. A 4.5-kV 1.2-kA IGBT module from ABB was considered as a power switch in the conducted case studies. It was observed that by increasing load PF in constant-impedance load, conduction power loss of high-frequency and top/bottom low-frequency IGBTs increase, whereas increasing the load PF decreases conduction power loss in high-frequency and top/bottom low-frequency antiparallel diodes as well as in middle low-frequency IGBTs and antiparallel diodes. In addition, increasing load PF in constant-impedance load does not increase conduction power loss considerably in both high-frequency and low-frequency switching-power-cells. Moreover, closed-form equations are derived for analytical determination of the switching power losses for ANPC-FCM converter using Kapteyn (Fourier-Bessel) series. According to obtained results, the maximum conduction power loss (occurring for $PF \approx 1$) and switching power loss of 12.1-MVA 6.6-kV three-phase nine-level (line-to-line) ANPC-FCM are roughly 38.55 and 49.9404 kW, respectively, while they are low as compared to the converter output power. In other words, total conduction power loss and switching power loss of the converter are 0.318% and 0.41%, respectively, that is 0.7313% of the converter output power. Based on the derived closed-form equations for conduction loss and switching loss calculation, a method is presented to analytically calculate the junction temperature of IGBTs and diodes and its effect on the conduction power loss for ANPC-FCM converter.

REFERENCES

[1] S. Rivera, S. Kouro, B. Wu, S. Alepuz, M. Malinowski, P. Cortes, and J. Rodriguez, "Multilevel direct power control—A generalized approach for grid-tied multilevel converter applications," *IEEE Trans. Power Electron.*, vol. 29, no. 10, pp. 5592–5604, Oct. 2014.

[2] J. Rodriguez, L. G. Franquelo, S. Kouro, J. I. Leon, R. C. Portillo, M. A. M. Prats, and M. A. Perez, "Multilevel converters: An enabling technology for high-power applications," *Proc. IEEE*, vol. 97, no. 11, pp. 1786–1817, Nov. 2009.

[3] L. Franquelo, J. Rodriguez, J. Leon, S. Kouro, R. Portillo, and M. Prats, "The age of multilevel converters arrives," *IEEE Ind. Electron. Mag.*, vol. 2, no. 2, pp. 28–39, Jun. 2008.

[4] J. Rodriguez, S. Bernet, P. K. Steimer, and I. E. Lizama, "A survey on neutral-point-clamped inverters," *IEEE Trans. Ind. Electron.*, vol. 57, no. 7, pp. 2219–2230, Jul. 2010.

[5] M. Malinowski, K. Gopakumar, J. Rodriguez, and M. A. Pérez, "A survey on cascaded multilevel inverters," *IEEE Trans. Ind. Electron.*, vol. 57, no. 7, pp. 2197–2206, Jul. 2010.

[6] H. Akagi, "Classification, terminology, and application of the modular multilevel cascade converter (MMCC)," *IEEE Trans. Power Electron.*, vol. 26, no. 11, pp. 3119–3130, Nov. 2011.

[7] V. Dargahi, A. K. Sadigh, G. K. Venayagamoorthy, and K. Corzine, "Hybrid double flying capacitor multicell converter and its application in grid-tied renewable energy resources," *IET Gener. Transm. Distrib.*, vol. 9, no. 10, pp. 947–956, Jul. 2015.

[8] D. Andler, R. Alvarez, S. Bernet, and J. Rodriguez, "Experimental investigation of the commutations of a 3L-ANPC phase leg using 4.5-kV–5.5-kA IGCTs," *IEEE Trans. Ind. Electron.*, vol. 60, no. 11, pp. 4820–4830, Nov. 2013.

[9] V. Dargahi, A. Khoshkbar Sadigh, M. Abarzadeh, M. R. A. Pahlavani, and A. Shoulaie, "Flying capacitors reduction in an improved double flying capacitor multicell converter controlled by a modified modulation method," *IEEE Trans. Power Electron.*, vol. 27, no. 9, pp. 3875–3887, Sep. 2012.

[10] V. Dargahi, A. Khoshkbar Sadigh, M. Abarzadeh, S. Eskandari, and K. Corzine, "A new family of modular multilevel converter based on modified flying-capacitor multicell converters," *IEEE Trans. Power Electron.*, vol. 30, no. 1, pp. 138–147, Jan. 2015.

[11] V. Dargahi and S. Dargahi, "Analytical modelling of single-phase stacked multicell multilevel converters exploiting Kapteyn (Fourier–Bessel) series," *IET Power Electron.*, vol. 6, no. 6, pp. 1220–1238, Jul. 2013.

[12] M. Aleenejad, H. Iman-Eini, and S. Farhangi, "Modified space vector modulation for fault-tolerant operation of multilevel cascaded H-bridge inverters," *IET Power Electron.*, vol. 6, no. 4, pp. 742–751, Apr. 2013.

[13] A. K. Sadigh, V. Dargahi, and K. A. Corzine, "New multilevel converter based on cascade connection of double flying capacitor multicell converters and its improved modulation technique," *IEEE Trans. Power Electron.*, vol. 30, no. 12, pp. 6568–6580, Dec. 2015.

[14] M. Aleenejad, P. Moamaei, H. Mahmoudi, and R. Ahmadi, "Unbalanced selective harmonic elimination for fault-tolerant operation of three phase multilevel cascaded H-bridge inverters," in *Proc. IEEE Appl. Power Electron. Conf. Expo.*, 2015, pp. 1589–1594.

[15] A. Khoshkbar Sadigh, M. Abarzadeh, K. A. Corzine, and V. Dargahi, "A new breed of optimized symmetrical and asymmetrical cascaded multilevel power converters," *IEEE J. Emerg. Sel. Top. Power Electron.*, vol. 3, no. 4, pp. 1160–1170, Dec. 2015.

[16] P. Alemi and D.-C. Lee, "Power loss comparison in two- and three-level PWM converters," in *Proc. IEEE 8th Int. Conf. Power Electron. ECCE Asia*, 2011, pp. 1452–1457.

[17] S. Mohan and R. Naik, "Design approach for high power, medium voltage power conversion systems for wind turbines," in *Proc. 16th Eur. Conf. Power Electron. Appl.*, 2014, pp. 1–9.

[18] F. Blaabjerg, U. Jaeger, and S. Munk-Nielsen, "Power losses in PWM-VSI inverter using NPT or PT IGBT devices," *IEEE Trans. Power Electron.*, vol. 10, no. 3, pp. 358–367, May 1995.

[19] M. Schweizer, T. Friedli, and J. W. Kolar, "Comparative evaluation of advanced three-phase three-level inverter/converter topologies against two-level systems," *IEEE Trans. Ind. Electron.*, vol. 60, no. 12, pp. 5515–5527, Dec. 2013.

[20] C. Liu, B. Wu, N. R. Zargari, D. Xu, and J. Wang, "A Novel three-phase three-leg AC/AC converter using nine IGBTs," *IEEE Trans. Power Electron.*, vol. 24, no. 5, pp. 1151–1160, May 2009.

[21] Q. Tu and Z. Xu, "Power losses evaluation for modular multilevel converter with junction temperature feedback," in *Proc. IEEE Power Energy Society General Meeting*, 2011, pp. 1–7.

[22] O. S. Senturk, L. Helle, S. Munk-Nielsen, P. Rodriguez, and R. Teodorescu, "Power capability investigation based on electrothermal models of press-pack IGBT three-level NPC and ANPC VSCs for multimegawatt wind turbines," *IEEE Trans. Power Electron.*, vol. 27, no. 7, pp. 3195–3206, Jul. 2012.

[23] S. Rohner, S. Bernet, M. Hiller, and R. Sommer, "Modulation, losses, and semiconductor requirements of modular multilevel converters," *IEEE Trans. Ind. Electron.*, vol. 57, no. 8, pp. 2633–2642, Aug. 2010.

[24] L. Schwager, A. Tuysuz, C. Zwyssig, and J. W. Kolar, "Modeling and comparison of machine and converter losses for PWM and PAM in high-speed drives," *IEEE Trans. Ind. Appl.*, vol. 50, no. 2, pp. 995–1006, Mar./Apr. 2014.

[25] M. Hartmann, H. Ertl, and J. W. Kolar, "Current control of three-phase rectifier systems using three independent current controllers," *IEEE Trans. Power Electron.*, vol. 28, no. 8, pp. 3988–4000, Aug. 2013.

[26] M. Schweizer and J. W. Kolar, "Design and implementation of a highly efficient three-level T-type converter for low-voltage applications," *IEEE Trans. Power Electron.*, vol. 28, no. 2, pp. 899–907, Feb. 2013.
[27] D. Andler, R. Alvarez, S. Bernet, and J. Rodriguez, "Switching loss analysis of 4.5-kV–5.5-kA IGCTs Within a 3L-ANPC phase leg prototype," *IEEE Trans. Ind. Appl.*, vol. 50, no. 1, pp. 584–592, Jan./Feb. 2014.
[28] F. Krismer and J. W. Kolar, "Closed form solution for minimum conduction loss modulation of DAB converters," *IEEE Trans. Power Electron.*, vol. 27, no. 1, pp. 174–188, Jan. 2012.
[29] S. S. Fazel, S. Bernet, D. Krug, and K. Jalili, "Design and comparison of 4-kV neutral-point-clamped, flying-capacitor, and series-connected H-bridge multilevel converters," *IEEE Trans. Ind. Appl.*, vol. 43, no. 4, pp. 1032–1040, Jul./Aug. 2007.
[30] T. B. Soeiro and J. W. Kolar, "The new high-efficiency hybrid neutral-point-clamped converter," *IEEE Trans. Ind. Electron.*, vol. 60, no. 5, pp. 1919–1935, May 2013.
[31] H. Sepahvand, M. Khazraei, K. Corzine, and M. Ferdowsi, "Start-up procedure and switching loss reduction for a single-phase flying capacitor active rectifier," *IEEE Trans. Ind. Electron.*, vol. 60, no. 9, pp. 3699–3710, May 2013.
[32] P. Barbosa, P. Steimer, J. Steinke, M. Winkelnkemper, and N. Celanovic, "Active-neutral-point-clamped (ANPC) multilevel converter technology," in *Proc. Eur. Conf. Power Electron. Appl.*, 2005, pp. 1–10.
[33] F. Kieferndorf, M. Basler, L. A. Serpa, J.-H. Fabian, A. Coccia, and G. A. Scheuer, "ANPC-5L technology applied to medium voltage variable speed drives applications," in *Proc. Int. Symp. Power Electron. Electr. Drives Autom. Motion*, 2010, pp. 1718–1725.
[34] F. Kieferndorf, M. Basler, L. A. Serpa, J.-H. Fabian, A. Coccia, and G. A. Scheuer, "A new medium voltage drive system based on ANPC-5L technology," in *Proc. IEEE Int. Conf. Ind. Technol.*, 2010, pp. 643–649.
[35] S. Kouro, M. Malinowski, K. Gopakumar, J. Pou, L. G. Franquelo, J. Rodriguez, M. A. Pérez, and J. I. Leon, "Recent advances and industrial applications of multilevel converters," *IEEE Trans. Ind. Electron.*, vol. 57, no. 8, pp. 2553–2580, Aug. 2010.
[36] K. Wang, Z. Zheng, Y. Li, K. Liu, and J. Shang, "Neutral-point potential balancing of a five-level active neutral-point-clamped inverter," *IEEE Trans. Ind. Electron.*, vol. 60, no. 5, pp. 1907–1918, May 2013.
[37] Y. Jiao, S. Lu, and F. C. Lee, "Switching performance optimization of a high power high frequency three-level active neutral point clamped phase leg," *IEEE Trans. Power Electron.*, vol. 29, no. 7, pp. 3255–3266, Jul. 2014.
[38] J. Li, S. Bhattacharya, and A. Q. Huang, "A new nine-level active NPC (ANPC) converter for grid connection of large wind turbines for distributed generation," *IEEE Trans. Power Electron.*, vol. 26, no. 3, pp. 961–972, Mar. 2011.
[39] G. Tan, Q. Deng, and Z. Liu, "An optimized SVPWM strategy for five-level active NPC (5L-ANPC) Converter," *IEEE Trans. Power Electron.*, vol. 29, no. 1, pp. 386–395, Jan. 2014.
[40] A. M. Bazzi, P. T. Krein, J. W. Kimball, and K. Kepley, "IGBT and diode loss estimation under hysteresis switching," *IEEE Trans. Power Electron.*, vol. 27, no. 3, pp. 1044–1048, Mar. 2012.
[41] C. S. Edrington, O. Vodyakho, M. Steurer, S. Azongha, F. Fleming, and M. Krishnamurthy, "Power semiconductor loss evaluation in voltage source IGBT converters for three-phase Induction Motor drives," in *Proc. IEEE Veh. Power Propulsion Conf.*, 2009, pp. 1434–1439.
[42] S. Srinivas and V. T. Somasekhar, "Space-vector-based PWM switching strategies for a three-level dual-inverter-fed open-end winding induction motor drive and their comparative evaluation," *IET Electr. Power Appl.*, vol. 2, no. 1, pp. 19–31, Jan. 2008.
[43] A. M. Y Ghias, J. Pou, M. Ciobotaru, and V. G. Agelidis, "Voltage balancing strategy for a five-level flying capacitor converter using phase disposition PWM with sawtooth-shaped carriers," in *Proc. 38th Annu. Conf. IEEE Ind. Electron. Soc.*, 2012, pp. 5013–5019.
[44] J. Pontt, J. Rodriguez, R. Huerta, P. Newman, W. Michel, and C. L. Argandona, "High-power regenerative converter for ore transportation under failure conditions," *IEEE Trans. Ind. Appl.*, vol. 41, no. 6, pp. 1411–1419, Nov. 2005.
[45] T. Bruckner and S. Bernet, "Loss balancing in three-level voltage source inverters applying active NPC switches," in *Proc. IEEE 32nd Annu. Power Electron. Specialists Conf.* , 2001, vol. 2, pp. 1135–1140.
[46] R. Withanage and N. Shammas, "Series connection of insulated gate bipolar transistors (IGBTs)," *IEEE Trans. Power Electron.*, vol. 27, no. 4, pp. 2204–2212, Apr. 2012.
[47] Y. Abe and K. Maruyama, "Multi-series connection of high-voltage IGBTs," *Fuji Electr. J.*, vol. 8, pp. 1–4, 2002.
[48] S. Hong, V. Chitta, and D. A. Torrey, "Series connection of IGBT's with active voltage balancing," *IEEE Trans. Ind. Appl.*, vol. 35, no. 4, pp. 917–923, Jul./Aug. 1999.
[49] D. Ning, X. Tong, M. Shen, and W. Xia, "The experiments of voltage balancing methods in IGBTs series connection," in *Proc. Asia-Pacific Power Energy Eng. Conf.*, 2010, pp. 1–4.
[50] S. Zheng, Y. Wang, X. Wu, Z. Qian, and F. Z. Peng, "The voltage sharing of commercial IGBTS in series with passive components," in *Proc. IEEE Energy Convers. Congr. Expo.: Energy Convers. Innovation Clean Energy Future*, 2011, pp. 3008–3012.
[51] Z. Zhang, Z. Xu, and Y. Xue, "Valve losses evaluation based on piecewise analytical method for MMC-HVDC links," *IEEE Trans. Power Del.*, vol. 29, no. 3, pp. 1354–1362, Jun. 2014.
[52] S. Ceballos, J. Pou, J. Zaragoza, J. L. Martín, E. Robles, I. Gabiola, and P. Ibáñez, "Efficient modulation technique for a four-leg fault-tolerant neutral-point-clamped inverter," *IEEE Trans. Ind. Electron.*, vol. 55, no. 3, pp. 1067–1074, Mar. 2008.
[53] J. Pou, J. Zaragoza, S. Ceballos, M. Saeedifard, and D. Boroyevich, "A carrier-based PWM strategy with zero-sequence voltage injection for a three-level neutral-point-clamped converter," *IEEE Trans. Power Electron.*, vol. 27, no. 2, pp. 642–651, Feb. 2012.
[54] A. M. Y. Mohammad Ghias, J. Pou, and V. Agelidis, "On reducing power losses in stack multicell converters with optimal voltage balancing method," *IEEE Trans. Power Electron.* , vol. 30, no. 9, pp. 4682–4695, Sep. 2015.
[55] A. M. Y. Mohammad Ghias, J. Pou, and V. G. Agelidis, "Voltage balancing method for stacked multicell converters using phase-disposition PWM," *IEEE Trans. Ind. Electron.* , vol. 62, no. 7, pp. 4001–4010, Jul. 2015.
[56] A. M. Y. Mohammad Ghias, J. Pou, V. Agelidis, and M. Ciobotaru, "Optimal switching transitions based voltage balancing method for flying capacitor multilevel converters," *IEEE Trans. Power Electron.*, vol. 30, no. 4, pp. 1804–1817, Apr. 2015.
[57] U. Drofenik and J. Kolar, "A general scheme for calculating switching- and conduction-losses of power semiconductors in numerical circuit simulations of power electronic systems," in *Proc. Int. Power Electron. Conf.*, 2005, pp 1–7.
[58] A. D. Rajapakse, A. M. Gole, and P. L. Wilson, "Electromagnetic transients simulation models for accurate representation of switching losses and thermal performance in power electronic systems," *IEEE Trans. Power Deliv.*, vol. 20, no. 1, pp. 319–327, Jan. 2005.
[59] G. Fedele and D. Frascino, "Spectral analysis of a class of DC-AC PWM inverters by Kapteyn series," *IEEE Trans. Power Electron.*, vol. 25, no. 4, pp. 839–849, Apr. 2010.
[60] V. Dargahi, "Detailed and comprehensive mathematical modeling of flying-capacitor stacked multicell multilevel converters," *COMPEL Int. J. Comput. Math. Electr. Electron. Eng.*, vol. 33, no. 1, pp. 483–526, 2014.

Arash Khoshkbar Sadigh (S'09–M'15) received the B.S. and M.S. degrees (both with first Hons.) in electrical engineering from the University of Tabriz, Tabriz, Iran, in 2007 and 2009, respectively, and the Ph.D. degree in electrical engineering from the University of California-Irvine, Irvine, CA, USA, in 2014.

He was with AranNagshAra Consultant Engineering Company, Tabriz, from 2007 to 2010, where he was involved in the design of power transmission and distribution lines. During summer 2012 to 2013, he was an Intern with the RTDS Advanced Technology Laboratory, Southern California Edison. In 2015, he joined Extron Electronics as the Power Electronics Design Engineer. He is the author or coauthor of more than 60 journal and conference papers and one book chapter, and he holds one patent. His research interests include power electronics circuits, multilevel converters and their applications in power grid and system, power quality, and flexible ac transmission system devices.

Dr. Sadigh was selected by the University of Tabriz as the Distinguished Student in 2006. In 2007, he joined the Iran's National Elites Foundation as he ranked second in the National Entrance Exam for graduate study in electrical engineering with a major in power engineering. He received the Outstanding Presentation Award from the Annual IEEE Applied Power Electronics Conference and Exposition in 2013.

Vahid Dargahi (S'08) received the B.Sc. degree in electrical engineering majoring power, and the M.Sc. degree in electrical engineering majoring electric power systems and power electronics from the Iran University of Science and Technology, Tehran, Iran, in 2011. He is currently working toward the Ph.D. degree in electrical engineering with the Microgrid and Power Electronics Laboratory, Holcombe Department of Electrical and Computer Engineering, Clemson University, SC, USA.

He is a Member of Iran's National Elites Foundation. His current research and practical interests include mainly the areas of analysis, modeling, modulation, control, and design of power electronic converters (PECs), innovating novel topologies of PECs with a particular emphasis on high-power voltage/current-source multilevel converters, renewable energy harnessing, and real-time simulation of microgrid power systems utilizing real-time digital simulator machines.

Keith A. Corzine (S'92–M'97–SM'06) received the B.S.E.E., M.S.E.E., and Ph.D. degrees from the University of Missouri, Rolla, MO, USA, in 1997.

He taught at the University of Wisconsin, Milwaukee, WI, USA, the University of Missouri, Rolla, MO, USA, Missouri University of Science and Technology, MO, USA. He is currently a Professor at Clemson University, Clemson, SC, USA. His research interests include power electronics, motor drives, naval ship propulsion systems, and electric machinery. He has published more than 50 refereed journal papers, more than 100 refereed international conference papers, and holds three U.S. patents related to power conversion.

Dr. Corzine was the past Chair of the IEEE St. Louis Section.